A multiomics approach reveals RNA dynamics promote cellular sensitivity to DNA hypomethylation

Alex Y. Ge[1*], Abolfazl Arab[2,3,4*], Raymond Dai[3,4], Albertas Navickas[3,4,5,6], Lisa Fish[3,4,5,6], Kristle Garcia[3,4,5,6] , Hosseinali Asgharian[3,4,5,6], Hani Goodarzi[3,4,5,6#], Luke A. Gilbert[2,3,4#]

1 School of Medicine, University of California, San Francisco, San Francisco, CA, USA
2 Arc Institute, Palo Alto, CA
3 Department of Urology, University of California, San Francisco, San Francisco, CA, USA
4 Helen Diller Family Comprehensive Cancer Center, University of California, San Francisco, San Francisco, CA, USA
5 Department of Biochemistry and Biophysics, University of California, San Francisco, San Francisco, CA, USA
6 Bakar Computational Health Sciences Institute, University of California, San Francisco, San Francisco, CA, USA

* Equal contribution and co-first authors
# Co-corresponding and co-senior authors (Hani.Goodarzi@ucsf.edu and luke@arcinstitute.org)

Contributions

A.Y.G., L.A.G. and H.G. conceived and designed the experiments. A.Y.G., R.D., A.N., L.F. and K.G. performed the experiments. A.Y.G., H.G., A.A., L.A.G. and H.A. analyzed the screen and screen validation results. A.A. and H.G. integrated and analyzed the multiomics datasets. A.A., L.A.G., H.G. and A.Y.G. wrote the paper.

ABSTRACT

The search for new approaches in cancer therapy requires a mechanistic understanding of cancer vulnerabilities and anti-cancer drug mechanisms of action. Problematically, some effective therapeutics target cancer vulnerabilities that we do not understand and have poorly defined mechanisms of anti-cancer activity. One such drug is decitabine, which is a frontline therapeutic approved for the treatment of high-risk acute myeloid leukemia (AML). Decitabine is thought to kill cancer cells selectively via inhibition of DNA methyltransferase enzymes, but the genes and mechanisms involved remain unclear. Here, we apply an integrated multiomics and CRISPR functional genomics approach to identify genes and processes associated with response to decitabine in AML cells. Our integrated multiomics approach reveals RNA dynamics are key regulators of DNA hypomethylation induced cell death. Specifically, regulation of RNA decapping, splicing and RNA methylation emerge as critical regulators of decitabine killing. Our results provide insights into the mechanisms of decitabine anti-cancer activity in treatment of AML and identify combination therapies which could potentiate decitabine anti-cancer activity.

INTRODUCTION

Epigenetic dysregulation drives many of the hallmarks of cancer by enabling aberrant gene expression programs which underlie cancer cellular plasticity and tumor heterogeneity phenotypes that promote cancer initiation, progression, metastasis and drug resistance[1]. Indeed, one of the key findings of the genomics era in cancer biology has been that most cancer genomes are epigenetically abnormal and mutations in genes that regulate DNA methylation, such as *DNMT3A/B*, *TET1-3* and *IDH1/2*, are prevalent[2,3]. Together, these observations suggest that epigenetic dysregulation promotes cancer but may also represent a targetable vulnerability. As such, there has been substantial interest in the development of anti-cancer strategies which modulate cancer associated epigenetic programs and dependencies[4–6]. One such promising strategy which has shown success in the context of certain subtypes of acute myeloid leukemia (AML) is to inhibit the activity of key enzymes required for maintenance and regulation of DNA methylation by small molecule drugs, such as decitabine, resulting in global DNA hypomethylation. There is clear evidence of clinical benefit of decitabine treatment for AML patients who have cytogenetic abnormalities associated with unfavorable risk, *TP53* mutations or both (defined hereafter as high-risk AML patients)[7,8]. Unfortunately, despite this benefit, most AML patients eventually progress following decitabine treatment with a median overall survival of less than 1 year. Problematically, relatively little progress has been made on improving the clinical activity of DNA hypomethylating agents (HMA) such as decitabine in AML or other cancers largely because the molecular determinants of response to HMAs are unclear.

A recent clinical study of molecular determinants of response to decitabine in AML patients has suggested that mutations in *DNMT3A*, *IDH1/2* and *TET2* are not correlated with response to decitabine[8]. In the same study, it was noted that TP53 mutations are also not correlated with poor clinical response to decitabine. These findings are unusual in two ways. First, it had previously been hypothesized that tumors with mutations that drive aberrant DNA methylation profiles may be more susceptible to HMAs. Secondly, *TP53* mutations are generally associated with drug resistance and poor prognosis in many cancers, so it is unexpected that *TP53* mutations in AML do not play a role

in determining clinical outcomes following treatment with decitabine. This result suggests that decitabine's anti-cancer activity in AML occurs through a *TP53* independent mechanism. Given the central role *TP53* plays in canonical apoptotic *BCL2* family protein dependent programmed cell death, at one level this study appears to contradict recent clinical trial results in AML which demonstrated superior clinical outcomes from the combination of a HMA (azacytidine) and venetoclax, a *BCL2* inhibitor thought to drive programmed cell death in cancer cells[9]. One explanation that could explain both sets of clinical observations is that HMAs may drive cell death via an unknown *TP53* independent apoptotic pathway. A more robust understanding of decitabine's mechanisms of anti-cancer activity in *TP53*-mutant tumors could enable innovative therapeutic strategies and a better understanding of patients who do and do not respond robustly to HMAs. An alternate hypothesis for how HMAs kill cancer cells arises from the observation that treatment with HMAs results in accumulation of non-canonical transcripts including inverted SINE elements, endogenous retroviral elements and cryptic transcription start sites encoded in long terminal repeats which collectively act to induce immune activation[10–14].

To identify genes that modulate decitabine's anti-cancer activity in high-risk AML in an unbiased manner, we performed a genome-scale CRISPR genetic screen and integrated this data with multiomics measurements of decitabine response. Our results recapitulate multiple known factors which modulate response to decitabine, including *DCK*, *SLC29A1*, *MCL1* and *BCL2*[15–18,9,19–21], indicating the utility and robustness of our approach for interrogating the biology of decitabine in AML. Central to our study was the finding that epitranscriptomic RNA modification and RNA quality control pathways effectively modulate response to decitabine in AML. In short, biologically we have identified regulatory connections between DNA methylation, RNA methylation and RNA quality control pathways, and translationally we have identified unexpected and clinically actionable biomarkers and combination therapies which should potentiate decitabine's anti-cancer activity in the clinic.

RESULTS

A genome-wide CRISPRi screen in AML cells identifies genes modulating decitabine sensitivity and resistance

We set out to perform a genome-scale genetic screen using our previously described CRISPR interference (CRISPRi)[22,23] functional genomics platform to identify genes that regulate cancer cell response to decitabine (Figure 1A), a clinically approved HMA. For this, we used the HL-60 cell line, which is an established model of AML. The cell line is *TP53*, *NRAS* and *MYC* mutant and captures the biology of high-risk AML and more generally of an aggressive human cancer. To begin, we generated an HL-60 CRISPRi cell-line model that stably expressed the dCas9-BFP-KRAB fusion protein. We validated that the resulting CRISPRi HL-60 cell line, hereafter referred to as HL-60i, is highly active for targeted gene knockdowns (Figure S1A).

Decitabine (5-aza-2'-deoxycytidine) is a pro-drug that is converted intracellularly into 5-aza-2'-deoxycytidine monophosphate[16,18,21]. This nucleoside analogue is in turn incorporated into DNA during replication, where it is thought to irreversibly and covalently trap and inhibit DNA methyltransferases *DNMT1*/*DNMT3A*/*DNMT3B* (Fig 1A). Trapping of DNMTs renders them enzymatically inactive, resulting in global DNA hypomethylation and dysregulated gene expression. This broad reprogramming of the gene expression landscape results in cell cycle arrest or cell death through poorly characterized molecular mechanisms. At high doses, decitabine also causes DNA replicative stress and DNA damage. To further characterize decitabine's activity in an AML cell model, we used publicly available data[24] to analyze changes in genome-wide DNA methylation patterns in HL-60 cells treated for 120 hours with a low dose of decitabine. As expected, we observed global hypomethylation of CpG dinucleotides and hypomethylation of differentially methylated regions (DMRs) following treatment with decitabine. This confirms the expected activity of decitabine, a non-specific DNMT inhibitor, in AML cells (Figure S1B-D). As discussed above, there is a hypothesis raised by clinical results that perhaps decitabine induces *TP53* independent but *BCL2* family protein dependent apoptosis. To address this, we next assessed whether decitabine treatment induces caspase 3/7 dependent apoptosis in our HL-60 model. We observed a dose dependent increase in caspase 3/7 activation upon treatment with low concentrations of decitabine (Figure S1E). Together, our results indicate that decitabine induces *TP53*-independent apoptosis and DNA hypomethylation in a model of high-risk AML and further supports our notion that this model could provide insight into decitabine's mechanism(s) of action.

For the genome-scale CRISPRi screen design and all subsequent experiments, we chose to treat cells with a clinically relevant low dose of decitabine (100 nM)[25]. At this concentration, decitabine's anti-cancer activity is thought to predominantly arise due to global DNA hypomethylation rather than via DNA replication stress[26,27]. Genome-scale pooled genetic screens were performed by transducing HL-60i cells with a human genome-scale CRISPRi sgRNA library at a low multiplicity of infection such that a single sgRNA is expressed in most cells, and then cells were selected with puromycin to remove uninfected cells from the population (Figure 1B). In addition to time-zero samples, we also collected samples after growing the library in the presence and absence of decitabine (in biological duplicates). Next-generation sequencing was used to quantify the relative abundance of cells

expressing each sgRNA in each sample. We then used measurements across the entire library to calculate sgRNA- and gene-level phenotypic scores (Figure S2A). Results obtained from the replicate screens were highly correlated with high data quality in both the DMSO and decitabine experiments (Figure S2B-E and Table 1). As expected, analysis of our DMSO control CRISPRi screen identified 1147 essential genes (Mann-Whitney p-value < 0.05 and gamma score <−0.1), enriched for ontologies known to be required for cell viability, whose knockdown results in sgRNA depletion within the screen (Table 1). This set of hit genes, which are required for HL-60 cell growth and/or survival, includes the vast majority of positive control commonly essential genes, indicating our HL-60i cellular model is highly active and our CRISPRi screen performed as expected. Analysis of our decitabine screen data revealed 1293 genes (Mann-Whitney p-value < 0.05 and absolute value of rho score > 0.1) that modulate cellular response to decitabine (Figure 1C and Table 1). The large number of hit genes identified in this decitabine screen may reflect the pleiotropic nature of DNA methylation biology.

Initial inspection of top hits from our decitabine CRISPRi screen recapitulated a number of genes whose knockdown is known to impact drug resistance and sensitivity (Figure 1C and Table 1). For example, the number one resistance hit in our screen was *DCK*, which phosphorylates decitabine resulting in conversion of the pro-drug to the active drug. Another top resistance hit was *SLC29A1*, which is a solute carrier protein required for decitabine entry into cells. We also observed that knockdown of *BCL2* and *MCL1* sensitizes HL-60i to decitabine, as expected from the clinical literature which suggests decitabine induces *BCL2* family protein mediated cell death.

RNA dynamics modulate response to DNA hypomethylation induced by decitabine in AML cells

Buoyed by these positive endogenous controls, we next examined the remaining CRISPRi hits to search for new biological insights and to generate hypotheses on the molecular mechanisms of decitabine action. First, we noted that the pathway-level analysis[28–30] of our screen identifies RNA metabolic pathways as a top-scoring enriched term (Figure S2F and Table S1). Further manual analysis of these top hits revealed a strong enrichment for two specific RNA biological processes (Table 1 and S1). Specifically, we observed that repression of RNA decapping enzymes such as *DCP1A*, *DCP2* and *DCPS* sensitizes HL-60 to decitabine (Figure 1C and Table 1). We also observed that repression of genes that regulate RNA methylation marks, specifically N^6-methyladenosine or m^6A promoted resistance to decitabine (Figure 1C and Table 1). Together, these observations suggest that modulation of specific RNA regulatory pathways is a key determinant of response to DNA hypomethylation induced by decitabine. To independently validate the results from our screen, we chose 10 hit genes from our decitabine CRISPRi screen (2 sgRNAs/gene) and used a mixed competition fluorescence cell survival CRISPRi knockdown assay to measure how perturbation of individual genes modulates response to decitabine. Our validation experiments demonstrated the reproducibility of our CRISRPi genome-scale screen measurements across all the resistance and sensitivity genes tested (Figure 1D-F). Of note, we observed that repression of *PTEN*, a widely established tumor suppressor gene that is commonly mutated in cancer, sensitized HL-60 cells to decitabine. This implies that patients with loss-of-function *PTEN* mutant tumors may respond more robustly to decitabine (Figure 1E).

We were intrigued by the connection between decitabine and RNA decapping quality control processes. To begin, we confirmed that repression of *DCP2* sensitizes cells to decitabine (Figure 1E). We further tested that RNA decapping is a pro-survival dependency by combining RG3039, a clinical grade chemical inhibitor of *DCPS*, with decitabine[31–33]. We observed the combination of decitabine and RG3039 had synergistic anti-cancer activity in two independent AML cell models (Figure S3A-B). We also observed that the combination of decitabine and RG3039 synergistically induced caspase 3/7 activation and cell cycle arrest in HL-60 (Figure 1G-H). Lastly, we profiled the transcriptional consequences of treating cells with DMSO, decitabine alone, RG3039 alone or decitabine and RG3039 together. Because previous literature has demonstrated HMAs can induce expression of endogenous retroviral elements, we mapped both protein coding transcript expression and ERV transcript expression. We observed that treatment with decitabine or RG3039 alone drives a transcriptional response (Figure S3C-D), and that the combination of decitabine with RG3039 induces transcriptional responses shared with the single drug conditions but also drug combination specific transcriptional changes (Figure S3C-D). Gene ontology analysis comparing decitabine to decitabine plus RG3039 or DMSO to decitabine plus RG3039 demonstrated up regulation of term enrichment for biological processes such as myeloid differentiation and immune function, as well as down regulation for biological processes relating to methylation and protein translation (Figure S3E). For example, we observed the upregulation of positive regulators of TNFα cytokine production specifically in the decitabine plus RG3039 condition relative to decitabine alone (Figure 1I). Prior studies have shown decitabine treatment alone can induce expression of atypical transcripts which in turn can induce an inflammatory response[10,34]; our analysis of ERV transcriptional changes demonstrated that the combination of decitabine plus RG3039 strongly induced specific ERV transcripts, such as PABL_A (chr9:9641512-9642657)[35], relative to DMSO or each single drug alone (Figure 1J). Notably, most ERVs do not change expression, and changes in expression are often not concordant across families or classes of ERVs (Figure S3F-G). Together, this data suggests that a new combination therapy consisting either of two drugs (decitabine and an RNA decapping inhibitor) or three drugs (decitabine, venetoclax and a RNA decapping inhibitor) could have synergistic activity for the treatment of AML and potentially have a unique mechanism of action. Given the known toxicity of venetoclax[36], a decitabine/RG3039 combination therapy could have lower toxicity while maintaining a strong survival benefit for patients.

DNMT1 inhibition in AML cells results in hypermethylation of mRNA transcripts

As highlighted above, we observed that repression of multiple genes encoding m^6A methylation machinery promotes cellular resistance to decitabine (Figure 1C and 1F). Top hits included the m^6A-writer *METTL3*, the m^6A-reader *YTHDF2* and the methyltransferase complex components *ZC3H13* and *CBLL1*. We validated that repression of *METTL3*, *YTHDF2*, and *ZC3H13* promotes resistance to DNMT inhibition by decitabine treatment in HL-60i over a time course using a mixed competition fluorescence cell survival CRISPRi knockdown assay (Figure 2A). This result suggests regulation of RNA methylation modulates AML cell survival upon treatment with decitabine.

To systematically examine the molecular effect of decitabine treatment on m^6A RNA methylation, we next performed methylated RNA immunoprecipitation sequencing (MeRIP-seq)[37], a method for

detection of m^6A modifications (Figure 2B). To assess the quality of this dataset, we first performed peak calling in control DMSO-treated samples followed by downstream analysis to recapitulate known features of the RNA modification sites across the transcriptome. We also performed a motif-enrichment analysis[38] to ensure the enrichment of the RGAC ([AG]GAC) motif sequence, a known m^6A motif [39], among predicted peaks (Figure 2C). Finally, we confirmed the preferential localization of RNA methylation peaks near the stop codon (Figure 2D), which is consistent with prior literature[40].

To then identify decitabine-induced hyper- and hypomethylated sites, we performed differential RNA methylation analysis to compare treatment with decitabine to DMSO controls[41]. Interestingly, we observed a general RNA hypermethylation signal across the transcriptome upon decitabine treatment (Figure 2E and Table 2). There are 4626 significant bins reported differential loci at FDR < 0.1 and log fold change (logFC) > 0.5. Specifically, our analysis identified 2064 decitabine induced hypermethylated peaks (logFC >1 and p-value <0.005 and Figure 2F) but only 1399 hypo methylated peaks (logFC <−1 and p-value <0.005 and Figure 2G). Taken together, our findings show that treatment of AML cells with decitabine results in global CpG DNA hypomethylation along with a concomitant increase in m^6A RNA methylation, and that HMA anti-cancer activity in AML cells is modulated by genes that regulate m^6A RNA methylation.

A multiomics approach identifies genes potentially regulated through m^6A

RNA methylation has been implicated in various aspects of the RNA life cycle in the cell[42], from RNA processing[43] to RNA stability[44] to translation[45,46], and more recently, crosstalk between epitranscriptome and epigenome[47–50]. To further understand the connection between global DNA hypomethylation and RNA dynamics in AML cells, we set out to interrogate, via an integrated multiomics approach, the effects of decitabine-induced RNA hypermethylation on AML cells. Here, we aimed to integrate comparisons between treatment with decitabine or DMSO from the following datasets: RNA-seq for differential gene expression and RNA stability, MeRIP-seq for RNA methylation, Ribo-seq for protein translation efficiency, and genome-scale CRISPRi functional genomics screening data. We first performed an RNA-seq time course experiment in the HL-60 AML model (Figure S4A) at 6, 72 and 120 hours following treatment with decitabine or DMSO. We used this data to perform differential gene expression analysis across conditions. We also used REMBRANDTS, a method we have previously developed for differential RNA stability analysis, to estimate post-transcriptional modulations in relative RNA decay rates[51–56] (Figure 3A-B). We performed gene set enrichment analysis[57]of differential mRNA stability and expression across all three time points for the HL-60 cell line (Figure S4B-C). For expression, we observed enrichment for largely expected ontologies, such as immune receptor activity and regulation of cell killing[10,12,14,19,34]. Interestingly, for post-transcriptional modulations in RNA stability, we observed previously unexplored terms, such as sterol biology, which we will further discuss below. Moreover, to also capture patient heterogeneity, we also performed RNA-seq on a panel of five other AML cancer cell lines treated with decitabine or DMSO. Across all six AML cell lines, we observed that decitabine treatment induced widespread changes in RNA transcript abundance and RNA stability with varying degrees of concordant RNA expression and stability changes (Figure 3C-D).

Given that RNA m^6A methylation marks have been previously implicated in translational control[45,58], we used Ribo-seq to measure changes in the translational efficiency landscape of HL-60 cells treated with decitabine or DMSO. Treatment with decitabine had little effect on translation efficiency, and we did not observe a concerted change in the translation efficiency of hypermethylated mRNAs (Figure S5). In other words, changes in translation efficiency of mRNAs that are differentially methylated in decitabine-treated cells are not likely to be responsible for cellular sensitivity to this drug.

Having ruled out translational control as the mechanism through which RNA methylation may be involved, we next sought to identify genes whose RNA hypermethylation drives cellular sensitivity to decitabine through other post-transcriptional regulatory programs. Since m^6A RNA methylation is shown to reduce RNA stability and expression[59,60], we intersected our set of decitabine-induced hypermethylated genes with those that are downregulated in decitabine treated cells, and their lower expression is associated with higher sensitivity to decitabine in our functional CRISPRi screen (Figure 3E). In this analysis, we observed ten genes that were decitabine sensitizing hits in the CRISPRi screen, showed RNA hypermethylated peaks, and were downregulated upon decitabine treatment (Figure 4A). We observed that these genes collectively regulate nuclear processes (*INTS5*, *INO80D*, *ZNF777*, *MYBBP1A*, *RNF126*, *RBM14-RBM4*)) or metabolism (*SQLE*, *DHODH*, *PMPCA*, *SLC7A6*). We were especially interested in *SQLE*, which is thought to be the enzyme that is rate limiting for sterol biogenesis[61,62], highlighted above as downregulated upon decitabine treatment. We selected *SQLE* and *INTS5* from the above analysis (Figure S6A-B) and validated that their mRNA abundance is decreased and m^6A methylation is increased in HL-60 cells following treatment with decitabine (Figure 4B-C). Consistently, we observed that *SQLE* and *INTS5* pre-mRNA levels do not change, showing that the decreased mRNA levels are not due to a decrease in transcription. These results suggest we have identified a small number of mRNAs that are likely downregulated due to increased m^6A methylation following decitabine treatment and that these same genes are functionally important for cellular response to decitabine.

To extend our observations, we also identified genes that (i) were downregulated upon decitabine treatment across our six AML cell line panel, (ii) sensitizing hits in our HL-60 CRISPRi screen, and (iii) showed hypermethylated peaks upon decitabine treatment in our MeRIP-seq HL-60 data (Figure 4D). We also identified genes that (i) showed reductions in their mRNA stability across our six cell line panel, (ii) were sensitizing hits in our HL-60 CRISPRi screen, and (iii) showed hypermethylated peaks upon decitabine treatment in our MeRIP HL-60 data (Figure 4E). Although this analysis converges on a very small number of genes, we were nevertheless intrigued by the possibility that several nominated genes could serve as a link between RNA methylation and the cell death induced by decitabine. This analysis reveals *BCL2* (Figure 1C-E, Figure 4E and Figure S6D) as a gene whose mRNA levels are potentially negatively regulated by RNA methylation and whose knockdown sensitizes cells to decitabine. Together these data suggest RNA methylation negatively regulates *BCL2* transcript abundance and downregulation of *BCL2* mRNA levels increases cellular sensitivity to decitabine induced cell death.

DISCUSSION

Our experiments identify previously known and unknown genes and pathways that modulate response to decitabine, a clinically approved HMA. Our results unexpectedly reveal a key role for RNA dynamics in modulating the cellular response to DNA hypomethylation induced by decitabine.

Specifically, we observed that genes which are thought to regulate mRNA decapping promote cellular resistance to decitabine. One hypothesis for why loss of RNA decapping enzyme activity sensitizes AML cells to decitabine is that this RNA quality control pathway becomes an induced dependency upon decitabine treatment due to repressed or aberrant transcripts that accumulate upon decitabine-induced DNA hypomethylation. Alternatively, some RNA decapping proteins are also key regulators of splicing, so it may be that this biology is more complex with respect to transcription than currently appreciated[63,64].

We also observed that genes which are thought to both write and read m^6A RNA methyl marks promote sensitivity to decitabine. Although many functions of m^6A have been identified, here we demonstrate a drug phenotype associated with m^6A biology. Given all known human methyltransferase enzymes use S-adenosyl methionine (SAM) as a cofactor for transfer of methyl groups, an intriguing hypothesis arises in which treatment of cells with decitabine results in global inhibition of DNMTs, resulting in increased SAM levels and subsequently hypermethylation of mRNAs leading to cell death. To our knowledge, cross talk between methyl transferase enzymes with different macromolecular substrates is not known, and this hypothesis may merit further investigation.

Our efforts have several translational implications for AML patients who are treated with decitabine. First, we nominate loss of *PTEN* as a biomarker that may identify patients who are more likely to benefit from decitabine. Second, we also experimentally confirm that decitabine induces *TP53* independent apoptosis in our experimental models, which has important implications for future therapeutic strategies. In line with this, our results genetically re-nominate a clinically efficacious combination therapy of decitabine and a *BCL2* inhibitor, which together likely induce synergistic apoptosis. Lastly, we nominate the combination of decitabine and RG3039, an RNA decapping inhibitor, as a new combination therapy for the potentiation of HMAs in AML treatment.

Successful anti-cancer combination therapies must show increased anti-cancer activity relative to a monotherapy without concomitant problematic increases in toxicity. Thus, a key consideration for our proposed combination therapy of decitabine and RG3039 is the potential for toxicity. Surprisingly to us, three lines of evidence show that RNA decapping activity is not an essential cellular process in all human cells. First, humans harboring germline bi-allelic *DCPS* loss-of-function mutations are viable with normal hematopoiesis[65]. Second, under normal growth conditions, *DCP1A*, *DCP2* and *DCPS* are not strongly essential genes in our data or in the Cancer Dependency Map. Lastly, RG3039, the *DCPS* inhibitor used in our studies, was originally developed to treat spinal muscular atrophy. Phase 1a and Phase 1b clinical trials showed that RG3039 was well tolerated and could robustly inhibit *DCPS* activity, however further trials were not pursued in SMA patients due to lack of efficacy[31]. Together, these results suggest that inhibition of *DCPS* alone is

likely to be non-toxic and suggests the possibility that a decitabine and RG3039 combination therapy could show increased anti-cancer activity with tolerable toxicity.

Lastly, HMAs with alternate mechanisms of action are likely to enter the clinic for the treatment of AML and potentially other cancers, and so our results may provide insight into this class of anti-cancer drugs.

ACKNOWLEDGEMENTS

We would like to thank members of the Goodarzi and Gilbert labs for helpful discussions and assistance, including Dr. Becky Xu Hua Fu, Dr. Benedict Choi, Laine Goudy, and Tanvi Joshi. We also thank Dr. Felix Krueger for helping A.A. troubleshoot Bismark. L.A.G. is funded by an NIH New Innovator Award (DP2 CA239597), a Pew-Stewart Scholars for Cancer Research award and the Goldberg-Benioff Endowed Professorship in Prostate Cancer Translational Biology. H.G. is an Era of Hope Scholar (W81XWH-2210121) and supported by R01CA240984 and R01CA244634. Sequencing was performed at the UCSF CAT, supported by UCSF PBBR, RRP IMIA and NIH 1S10OD028511-01 grants.

COMPETING INTERESTS

A.Y.G. and A.A. declare no competing interests. L.A.G has filed patents on CRISPR functional genomics, has worked with the UCSF/UC Berkeley/GSK Laboratory for Genomics Research on DNMT1 inhibitors and is a co-founder of Chroma Medicine.

METHODS

Cell culture and reagents

HL-60, KG-1 and THP-1 cells were obtained from the American Type Culture Collection. OCI-AML2 and OCI-AML3 cells were obtained from the Leibniz Institute DSMZ (German Collection of Microorganisms and Cell Cultures). MOLM-14 cells were obtained from the Shannon Lab at the University of California, San Francisco (UCSF). HEK-293T cells were obtained from the Weissman Lab at UCSF. HL-60, OCI-AML2, OCI-AML3 and KG-1 cells were cultured in Iscove's Modified Dulbecco's Medium (Gibco) supplemented with 20% fetal bovine serum (Seradigm), 100 U/mL penicillin (Gibco), 100 ug/mL streptomycin (Gibco) and 0.292 mg/mL glutamine (Gibco). MOLM-14 and THP-1 cells were cultured in RPMI-1640 medium (Gibco) supplemented with 20% FBS, penicillin, streptomycin and glutamine. HEK-293T cells were cultured in Dulbecco's Modified Eagle Medium (Gibco) supplemented with 10% FBS and penicillin, streptomycin and glutamine. All cell lines were grown at 37°C and 5% CO_2 and were tested for mycoplasma contamination using the MycoAlert PLUS Mycoplasma Testing Kit (Lonza) according to the manufacturer's instructions.

Decitabine powder was obtained from Selleck Chemicals and stored at -20°C. A stock solution of decitabine was created by reconstituting decitabine powder in dimethyl sulfoxide (DMSO) at a final concentration of 10 mM. The stock solution was aliquoted and stored at -80°C until experimental use. RG3039 was obtained from MedChemExpress.

DNA transfections and lentivirus production

HEK-293T cells were transfected with pMD2.G, pCMV-dR8.91 and a transfer plasmid using the TransIT-LT1 Transfection Reagent (Mirus Bio) and 8 ng/uL polybrene. Culture medium was exchanged with fresh medium supplemented with ViralBoost (Alstem) one day post-transfection. Lentiviral supernatant was collected, filtered through a 0.44 µm filter (Millipore) and used fresh (for CRISPRi screening) or concentrated via ultracentrifugation at 25,000 rpm for 90 minutes and frozen (for all other methods) three days post-transfection.

CRISPRi screen

CRISPRi cell line generation

HL-60 cells were transduced with Ef1a-dCas9-BFP-KRAB and sorted twice for BFP positive cells on a BD FACS Aria III. Sorted cells were diluted to single cell concentration (5, 1 or 0.2 cells per well) and plated into 96-well plates. Individual clones were expanded and assayed for CRISPRi activity by transducing sgRNAs targeting five essential genes (PLK1, HSPA9, AARS, POLR1D, DNAJC19) and assessing for relative depletion of GFP (i.e., sgRNA positive cells) via flow cytometry between day 3 and day 9 post-transfection. The clone with the highest relative GFP depletion was selected to be the HL-60 CRISPRi cell line for downstream experiments.

CRISPRi screen experimental procedure

Genome-scale CRISPRi screens were performed similarly to those previously described[22]. The human CRISPRi-v2 sgRNA library (top 5 sgRNAs per gene) was transduced into HL-60 CRISPRi cells at 250-fold coverage. Cells were resuspended in lentiviral supernatant with 8 µg/mL polybrene in 6-well plates and centrifuged at 1000 *g* for 2 hours at room temperature. Cells were resuspended into fresh medium following spinfection. 72 hours following infection, cells were seeded at 1,000,000 cells/mL for puromycin selection (1 ug/mL). Following puromycin selection, "time-zero" samples were harvested at 500x library coverage. The remaining cells were divided into two conditions, DMSO and decitabine, two replicates per condition. For the decitabine condition, cells were treated with 100 nM decitabine every 24 hours for 72 hours. Cells were grown in T150 flasks (Corning) and split when appropriate while maintaining 500x coverage. After 19 days of growth, cells were harvested at 500x coverage. Genomic DNA was isolated from all samples and the sgRNA-encoding region was enriched, amplified and processed for sequencing on the Illumina HiSeq 4000 (50 base pair single end reads) as previously described[66,67].

CRISPRi screen computational analysis

Sequencing reads were trimmed, aligned to the human CRISPRi-v2 sgRNA library and counted using a previously described pipeline (https://github.com/mhorlbeck/ScreenProcessing). Growth (γ) and drug sensitivity/resistance (ρ) phenotypes were calculated based on sgRNA frequencies across conditions[22,68]. Gene phenotypes were calculated by taking the mean of the top three sgRNA phenotypes per gene by magnitude. Gene phenotype p-values were calculated using the Mann-Whitney test comparing the gene-targeting sgRNAs with a set of non-targeting control sgRNAs. For genes with multiple annotated transcription start sites (TSS), sgRNAs were first clustered by TSS, and the TSS with the smallest Mann-Whitney p-value was used to represent the gene. Hits were defined as genes with a phenotype Z-score greater or equal to 6. Z-scores were calculated by dividing the gene phenotype by the standard deviation of the non-targeting sgRNA phenotypes[22].

To assess pathway-level enrichment of gene phenotypes in the CRISPRi screen, we used blitzGSEA[28], a Python package for the computation of Gene Set Enrichment Analysis (GSEA) (https://github.com/MaayanLab/blitzgsea). We obtained gene ontology (GO)[30] gene sets from MSigDB[30,69,70] (version 7.4.) and then conducted two separate analyses: (1) To identify smaller[29], focused pathways associated with drug sensitivity or resistance, we performed GSEA analysis on genes ranked by ρ phenotype and defined minimum and maximum thresholds for gene set size when running the `gsea` function (`min_size=15` and `max_size=150`). Thus, positive normalized enrichment scores (NES) corresponded to gene sets enriched among positive ρ phenotypes (i.e., resistance phenotypes) and negative NES corresponded to gene sets enriched among negative ρ phenotypes (i.e., sensitivity phenotypes). (2) To identify broader pathways associated with drug response irrespective of ρ phenotype direction, we performed GSEA analysis on genes ranked by 1 – Mann-Whitney p-value (calculated for each ρ phenotype as above) and set a minimum threshold for gene set size (i.e., `min_size=200`). Then we only report positive normalized enrichment scores (NES) that represent gene sets enriched by more significant Mann-Whitney p-value for the gene set's ρ phenotype.

Individual sgRNA validation

Individual sgRNAs were validated using a competitive growth assay as previously described[22]. Briefly, sgRNA protospacers with flanking BstXI and BlpI restriction sites were cloned into the BstXI/BlpI-digested pCRISPRia-v2 plasmid (Addgene #84832). Protospacer sequences are listed in Table 1. Individual sgRNA vectors (including a non-targeting control sgRNA) were then packaged into lentivirus as described above and transduced into HL-60 CRISPRi cells in duplicate. Three days after transduction, cells were treated with DMSO or 100 nM decitabine. The proportion of sgRNA-expressing cells was measured by flow cytometry on an LSR II (BD Biosciences) gating for GFP expression. The individual sgRNA phenotype was calculated by dividing the fraction of sgRNA-expressing cells in the treated condition by the fraction of sgRNA-expression cells in the untreated condition.

Reanalysis of public bisulfite sequencing data in HL-60 cells

Shareef et. al, as part of a study to introduce their extended-representation bisulfite sequencing method, treated HL-60 cells with DMSO (GSM4518676) or 300 nM decitabine (GSM4518677) and harvested cells after 5 days[24]. Raw FASTQ files were downloaded using the SRA Toolkit. TrimGalore[71] and Bismark[72] were used to preprocess and map bisulfite-treated reads to the h38 reference genome and subsequently call cytosine methylation. We followed the Bismark standard pipeline, which includes four functions: (1) running `bismark_genome_preparation`, (2) running `bismark`, (3) running `deduplicate_bismark` and (4) running `bismark_methylation_extractor` to extract context dependent (CpG/CHG/CHH) methylation.

Differential CpG DNA methylation analysis was performed using the methylKit R package[73]. CpG methylation data from Bismark was imported and the `getMethylationStats` function was used to calculate descriptive statistics. To search for differentially methylated tiles, the `tileMethylCounts` function was used with options `win.size=1000` and `step.size=1000`. Differentially methylated regions (DMRs) scored by % methylation difference and q-value were calculated using the `calculateDiffMeth` function. A one-sample, one-sided (lower-tail) t-test was used to test for statistically significant global DNA hypomethylation.

DCPS and RG3039 drug synergy experiments

Cell viability assay and Bliss excess score calculation

Cells were seeded into 96-well plates at 100,000 cells/mL in duplicate and were treated with decitabine (seven-point 1:3 dilution series from 0.5 uM to 0.002 uM), RG3039 (seven-point 1:4 dilution series from 10 uM to 0.010 uM) or the combination of both drugs at all possible dose combinations. Control cells treated with DMSO were counted at day 3, and all cells were split at the ratio required to dilute control cells to a concentration of 100,000 cells/mL. Raw fluorescence units (RLUs) were assessed at day 3, day 5 and day 7 for each condition using the CellTiter-Glo (CTG) luminescence-based assay (Promega). Diluted CTG reagent (100 uL 1:4 CTG reagent to PBS) was added to cells (100 uL) and the mixture was pipetted up and down to ensure complete cell lysis. Luminescence was then assayed using a GloMax Veritas Luminometer (Promega).

To calculate the proportion of viable cells, RLUs from the CTG assay were averaged between replicates and normalized to the DMSO control. The proportion of inhibited cells was calculated as one minus the proportion of viable cells. Drug synergy was determined by calculating the Bliss excess score (Bliss 1956)[74], i.e.

$$Bliss\ excess = I_{AB} - \hat{I}_{AB}$$

where I_{AB} represents the observed proportion of inhibited cells at drug doses A and B and $\hat{I}_{AB}$ represents the expected proportion of inhibited cells assuming Bliss independence, i.e.

$$\hat{I}_{AB} = I_A + I_B - (I_A \times I_B)$$

Cleaved caspase 3/7 assay

Cells were seeded into 24-well plates at 100,000 cells/mL in triplicate and were treated with decitabine (50 nM, 100 nM or 200 nM on days 0, 1 and 2) with and without RG3039 (2 uM on day 0). Cells were harvested on day 5 and the proportion of apoptotic cells was assessed using the NucView 488 Caspase-3 Assay Kit (Biotium) according to the manufacturer's instructions and an Attune NxT flow cytometer (Thermo Fisher Scientific) gating on the BL-1 channel.

Cell cycle assay

Cells were seeded into 24-well plates at 100,000 cells/mL in triplicate and were treated with decitabine (50 nM, 100 nM or 200 nM on days 0, 1 and 2) with and without RG3039 (2 uM on day 0). Cells (500,000–1,000,000 per sample) were harvested on day 5 and the proportions of cells in each phase of the cell cycle were assessed using the FxCycle Violet Kit (Thermo Fisher Scientific) and an Attune NxT flow cytometer (Thermo Fisher Scientific) gating on the VL-1 channel. Briefly, cells were washed once with PBS, fixed with 70% ethanol overnight at -20 ° C, pelleted, and then washed with PBS 1–2 times. Cells were then resuspended in 1 mL permeabilization buffer (PBS with 1% FBS and 0.1% Triton X-100) and 1 uL Fx cycle and stained for 30 minutes in the dark before being analyzed via flow cytometry.

RNA-seq experimental procedures

3' RNA-seq

3' RNA-seq was performed to assess differential gene expression following decitabine and/or RG3039 treatment. Cells were seeded into 6-well plates at 100,000 cells/mL in duplicate and were treated with decitabine (100 nM on days 0, 1 and 2), RG3039 (2 uM on day 0), both drugs or DMSO. On day 3, RNA was extracted using the RNeasy Mini Kit (Qiagen) according to the manufacturer's instructions. RNA-seq libraries were prepared using the QuantSeq 3′ mRNA-Seq Library Prep Kit FWD for Illumina (Lexogen) and assessed on a BioAnalyzer 2100 (Agilent) for library quantification and quality control. RNA-seq libraries were sequenced on an Illumina HiSeq 4000 using single-end, 50–base pair sequencing.

Stranded RNA-seq

Stranded RNA-seq was performed for experiments in which strand directionality was required for downstream analysis. Cells were seeded into 6-well plates at 100,000 cells/mL in duplicate or triplicate and were treated with decitabine (100 nM on days 0, 1 and 2) or DMSO. At 6, 72 and/or 120 hours, RNA was extracted using the RNeasy Mini Kit (Qiagen) according to the manufacturer's instructions. For HL-60 experiments, RNA-seq libraries were prepared using the ScriptSeq v2 kit (EpiCentre). Total RNA was depleted using RiboZero Gold (EpiCentre) and purified using the MinElute RNA kit (Qiagen). For all other cell lines, RNA-seq libraries were prepared using the SMARTer Stranded Total RNA Sample Prep Kit - HI Mammalian kit (Takara) due to retirement of the ScriptSeq v2 kit. Total RNA was depleted using the RiboGone module included with the SMARTer kit. All RNA-seq libraries were assessed on a BioAnalyzer 2100 (Agilent) for library quantification and quality control and sequenced on an Illumina HiSeq 4000 using single-end, 50–base pair sequencing.

Differential gene expression analysis

The Salmon-tximport-DESeq2 pipeline

We used a workflow hereafter referred to as the "Salmon-tximport-DESeq2 pipeline" to perform differential gene expression analysis. Salmon (version 1.2.1) was first used to quantify transcript abundance[53]. A Salmon index was generated using the GENCODE[75] (version 34) genome annotation, and subsequently the `salmon quant` tool was used with the `--validateMappings` option to calculate transcript abundances. Then, the R package tximport[52] was used to import Salmon results into R and perform data preparation. The `summarizeToGene` function was used to collapse transcript abundances to the gene level. From here, the R package DESeq2[51] was used for differential gene expression analysis. We first extracted normalized counts for each RNA-seq experiment using DESeq2 by running the `estimateSizeFactors` function and then the `counts` function with option `normalized=TRUE`. For each individual experiment, the DESeq2 statistical model was modified based on the experimental design. For experimental designs with multiple variables (e.g., multiple drug conditions, time points, etc.), we used the likelihood ratio test (LRT) to perform differential expression analysis. The LRT is conceptually similar to an analysis of variance (ANOVA) calculation in a linear regression model[76]. In these cases, we specified the model design in the `DESeq2` function as `~0 + variable1 + variable2 + variable1:variable2` and the argument `test=LRT`. In simple experimental designs with one variable (e.g., DMSO vs. decitabine treatment), DESeq2 was used with default options (i.e., a Wald test was used instead of a LRT). In these cases, the model design was specified as `~cond`. For experiments with batch effects, the model design was specified as `~cond + reps`.

Differential RNA stability analysis

The STAR-featureCounts-REMBRANDTS-limma pipeline

For analyses which required measurements of pre-mRNA and mature mRNA abundances from RNA-seq samples (i.e., differential RNA stability analysis), we used a workflow hereafter referred to as the "STAR-featureCounts-REMBRANDTS-limma pipeline". RNA-seq sequencing reads were first aligned to the hg38 reference genome using STAR[54] (version 2.7.3a). Then, featureCounts[77] was

used to quantify intron and exon level counts. Finally, REMBRANDTS was used to calculate mRNA stability as previously described[56] (https://github.com/csglab/REMBRANDTS). Briefly, the package estimates a gene-specific bias function that is subtracted from Δexon–Δintron calculations to provide unbiased mRNA stability measurements. To assess differential RNA stability changes, we used limma[55], which was designed for microarray experiments and serves a similar function to DESeq2, though it supports negative values (relevant for RNA stability analysis). The model designs used here are analogous to the designs for differential expression analysis described above.

RNA-seq iPAGE analysis

iPAGE run and downstream analysis pipeline

The iPAGE algorithm[57] was used for gene set and pathway enrichment analysis on differential RNA expression and stability results. MSigDB[30,69,70] (version 7.4.) was downloaded and modified to be compatible with iPAGE workflow. iPAGE was used in continuous mode, which accepts gene-level numeric values (e.g., logFCs) as input. Briefly, iPAGE quantizes differential measurements into equally populated bins and then, for every given geneset, calculates the mutual information (MI) between each cluster bin and a binary vector of pathway memberships for genes in a given gene set. The significance of each MI value is then assessed through a randomization-based statistical test and hypergeometric distribution to determine whether there is over or under representation of a gene set in each cluster bin. The final result is a p-values matrix in which rows are gene sets and columns are cluster bins (visualized as heatmaps). Code for all iPAGE analyses are available for download at https://github.com/abearab/pager.

RNA-seq workflows for specific experiments

Decitabine and RG3039 drug combination experiments

We performed 3' RNA-seq on HL-60 cells treated with DMSO, decitabine alone, RG3039 alone or both drugs for 72 hours in duplicate (see above for experimental procedures). Raw sequencing data were processed using our Salmon-tximport-DESeq2 pipeline (see above). DESeq2 was used to conduct differential gene expression analysis using a likelihood ratio test and the model design `~0 + decitabine + rg3039 + decitabine:rg3039`. Pathway enrichment was assessed using iPAGE (see above). For differential endogenous retrovirus (ERV) expression analysis, ERV data in GFF3 and FASTA formats were downloaded from the Human Endogenous RetroViruses Database[78,79] and then used in the Salmon-tximport-DESeq2 pipeline. Upregulated ERVs were defined as p-value < 0.05 and log2FC > 1, and downregulated ERVs were defined as p-value < 0.05 and log2FC < –1. The intersections of ERV data were visualized using UpSet plots in Python[80]. For PCA analysis, the `varianceStabilizingTransformation` function from the DESeq2 package was used to prepare counts. The `plotPCA` function was used to calculate PC variances as percentages. Finally, `ggplot2` was used to visualize a two-dimensional representation of the PCA analysis.

HL-60 time-series experiments

We performed stranded RNA-seq on HL-60 cells treated with decitabine for 6 hours, 72 hours and 120 hours in duplicate (see above for experimental procedures). Differential expression analysis was performed using our Salmon-tximport-DESeq2 pipeline (see above), using a likelihood ratio test and

a two-variable model design incorporating treatment condition (decitabine or DMSO) and time (6, 72 or 120 hours). Differential RNA stability analysis was performed using our STAR-featureCounts-REMBRANDTS-limma pipeline (see above). Pathway enrichment for differential expression and RNA stability data was assessed using iPAGE (see above).

AML cell line panel experiments

We performed stranded RNA-seq on KG-1, THP-1, OCI-AML2, OCI-AML3 and MOLM-14 cell lines treated with decitabine or DMSO for 72 hours in three replicates (see above for experimental procedures). Differential expression analysis was performed using our Salmon-tximport-DESeq2 pipeline (see above), using a Wald test. Differential RNA stability analysis was conducted using our STAR-featureCounts-REMBRANDTS-limma pipeline (see above). Pearson correlation tests from the Hmisc and corrplot R packages were used to assess correlation between differentially expressed genes in HL-60 and other AML cell lines. UpSet plots in Python[80] were used to identify and visualize genes across multiple cell lines that conferred drug sensitivity in the CRISPRi screen (ρ score < -0.1 and $p < 0.05$), were RNA hypermethylated (log2FC > 1 and $p < 0.05$) upon decitabine treatment, and either had decreased expression or RNA stability (log2FC < -0.1 and $p < 0.05$) upon decitabine treatment.

MeRIP-seq

Experimental procedure

We performed MeRIP-seq as previously described[37] on HL-60 cells treated with DMSO or decitabine for 72 hours in biological duplicates. First, 2 µg of the fragmented total RNA per sample was used for RNA immunoprecipitation (IP) with 5 µg of the anti-m^{6}A antibody (ABE572, Millipore). RNA-seq libraries from input and IP samples were prepared using the SMARTer Pico Input Mammalian v2 RNA-seq kit (Takara) and sequenced as SE50 runs on an Illumina HiSeq4000.

Alignment, peak calling and differential RNA methylation analysis

MeRIP-seq reads were aligned to the hg38 reference genome using STAR[54] (version 2.7.3a) with reference annotation GENCODE [75] (version 34). RADAR was used to perform peak calling and differential methylation analysis[41]. Both STAR and RADAR were used with default parameters. Differentially methylated peaks were defined as FDR < 0.1 and logFC > 0.5. Wilcoxon test and t-test functions were used to test for global m^{6}A hypermethylation. Metagene plots were visualized using the Guitar R/Bioconductor package[81]. For peak visualization across individual mRNA transcripts, the `plotGeneCov` function from the RADAR R package was used to generate coverage plots. Then, the Gviz R Bioconductor package[82] was used to draw detailed information for each mRNA transcript.

Motif enrichment analysis

First, the `exomepeak` function from the R package exomePeak[83] was used to call m^{6}A peaks. The following options were provided: `WINDOW_WIDTH = 50, SLIDING_STEP = 5, FRAGMENT_LENGTH = 150, FOLD_ENRICHMENT = 1`. Then, the sequences of predicted m^{6}A peaks were extracted using concepts described by Meng et. al[83]. Briefly, the `bed2bed` tool from the Computational Genomics Analysis Toolkit (with options `--method=merge --merge-by-name`) and the `getfasta` module from bedtools (with options `-name -s -split`) were used for sequence

extraction[84,85]. Finally, the FIRE algorithm was used in non-discovery mode for enrichment analysis of known m^6A motifs (i.e., RGAC or [AG]GAC) within peak sequences, compared to randomly generated sequences[38]. Scripts for all MeRIP-seq analyses are maintained as a GitHub project at https://github.com/abearab/imRIP.

Ribo-seq

Experimental procedure

Ribosome profiling was performed as previously described[86] in biological duplicates. Approximately $10x10^6$ cells were lysed in ice cold polysome buffer (20 mM Tris pH 7.6, 150 mM NaCl, 5 mM MgCl2, 1 mM DTT, 100 µg/mL cycloheximide) supplemented with 1% v/v Triton X-100 and 25 U/mL Turbo DNase (Invitrogen). The lysates were triturated through a 27G needle and cleared for 10 min at 21,000 *g* at 4°C. The RNA concentrations in the lysates were determined with the Qubit RNA HS kit (Thermo). Lysate corresponding to 15 µg RNA was diluted to 200 µl in polysome buffer and digested with 0.75 µl RNaseI (Epicentre) for 45 min at room temperature. The RNaseI was then quenched by 5 µl SUPERaseIN (Thermo).

Monosomes were isolated using MicroSpin S-400 HR (Cytiva) columns, pre-equilibrated with 3 mL polysome buffer per column. 100 µl digested lysate was loaded per column (two columns were used per 200 µl sample) and centrifuged 2 min at 600 *g*. The RNA from the flow through was isolated using the RNA Clean and Concentrator-25 kit (Zymo). In parallel, total RNA from undigested lysates were isolated using the same kit.

Ribosome protected footprints (RPFs) were gel-purified from 15% TBE-Urea gels as 17-35 nt fragments. RPFs were then end-repaired using T4 PNK (New England Biosciences) and pre-adenylated barcoded linkers were ligated to the RPFs using T4 Rnl2(tr) K227Q (New England Biosciences). Unligated linkers were removed from the reaction by yeast 5'-deadenylase (New England Biosciences) and RecJ nuclease (New England Biosciences) treatment. RPFs ligated to barcoded linkers were pooled, and rRNA-depletion was performed using riboPOOLs (siTOOLs) per the manufacturer's recommendations. Linker-ligated RPFs were reverse transcribed with ProtoScript II RT (New England Biosciences) and gel-purified from 15% TBE-Urea gels. cDNA was then circularized with CircLigase II (Epicentre) and used for library PCR. First, a small-scale library PCR was run supplemented with 1X SYBR Green and 1X ROX (Thermo) in a qPCR instrument. Then, a larger scale library PCR was run in a conventional PCR instrument, performing a number of cycles that resulted in ½ maximum signal intensity during qPCR. Library PCR was gel-purified from 8% TBE gels and sequenced on a SE50 run on an Illumina HiSeq4000.

Data preprocessing

The adapters in the sequencing reads were removed using cutadapt[87] (v3.1) with options `—trimmed-only -m 15 -a AGATCGGAAGAGCAC`. The PCR duplicates in the reads were collapsed using CLIPflexR[88] (v0.1.19). The UMIs for each read were extracted using UMI-tools [89] (v1.1.1) with the options `extract—bc-pattern=NN` for the 5' end and options `extract—3prime—bc-pattern=NNNNN` for the 3' end. Reads corresponding to rRNA and other non-nuclear mRNA were

removed by aligning out the reads using Bowtie2[90] (v2.4.2) on a depletion reference (rRNA, tRNA and mitochondrial RNA sequences). This depletion reference was built from the hg38 noncoding transcriptome (Ensembl[91,92] version 96). The reads that did not align to the depletion reference were aligned to the hg38 mRNA transcriptome (Ensembl version 96) using Bowtie2 with options `—sensitive—end-to-end—norc`. The mRNA transcriptome was built using the cDNA longest CDS reads of *Homo sapiens* downloaded from the Ensembl release version. The resulting reads were converted to BAM files and then sorted using samtools (v1.11). The duplicate reads in the sorted files were removed using UMI-tools (v1.1.1) with options `dedup`.

Differential translational efficiency (TE) analysis
Ribolog was used to compare translational efficiency across conditions[93] (https://github.com/goodarzilab/Ribolog). Briefly, Ribolog applies a logistic regression to model individual Ribo-seq and RNA-seq reads in order to provide estimates of logTER (i.e., logFC in TE) and its associated p-value across the coding transcriptome.

Multiomics data integration

To identify candidate genes among our multiomics datasets for downstream validation of our decitabine-m^{6}A model, we examined the intersection of three sets of genes: (1) sensitizing hits in the CRISPRi screen, defined as ρ score < -0.1 and $p < 0.05$; (2) genes with downregulated expression upon decitabine treatment, defined as log2FC < -0.1 and $p < 0.05$; (3) genes with RNA hypermethylation upon decitabine treatment, defined as logFC > 1 and $p < 0.05$. Intersections between sets were visualized through a Venn diagram in Python.

Quantitative RT-PCR

RNA isolation
Total RNA for quantitative RT-PCR assays was isolated using the Quick-RNA Microprep kit (Zymo) with on-column DNase treatment per the manufacturer's protocol.

Quantitative RT-PCR
Transcript levels were measured using quantitative RT-PCR by reverse transcribing total RNA to cDNA (Maxima H Minus RT, Thermo Fisher Scientific), then using fast SYBR green master mix (Applied Biosystems) or Perfecta SYBR green supermix (QuantaBio) per the manufacturer's instructions. HPRT1 was used as an endogenous control.

INTS5 primers
Exon-junction forward primer 5'–GGGATGTCCGCGCTGTG– 3' and reverse primer 5'–GGACAGCTCCTGAGCACTGA–3'. *Exon-intron* forward primer 5'–GGGATGTCCGCGCTGTG–3' and reverse primer 5'–AGTTCTCGAGGTAGGATCCGGGT–3'. *Predicted m^{6}A hypermethylated loci* forward primer 5'–TGCTGTCTGAGTTTATCCGGGCCA–3' and reverse primer 5'–TGGACCATGCACTAATCACAGGT–3'.

SQLE primers

Exon-junction forward primer 5'–CCCAGTTCGCCCTCTTCTCGGA– 3' and reverse primer 5'–GGTTCCTTTTCTGCGCCTCCTGG–3'. *Exon-intron* forward primer 5'–CCCAGTTCGCCCTCTTCTCGGA–3' and reverse primer 5'–ACCTGCCGCCTTTTGCAATTCA–3'. *Predicted m^6A hypermethylated loci* forward primer 5'–TTACTGGAGTCTGGCCGGCTCT–3' and reverse primer 5'–CGAGTGGGTTTAAGGTTCTCCCCA–3'.

Code availability

Code for iPAGE and MeRIP-seq analyses are publicly available at https://github.com/abearab/pager and https://github.com/abearab/imRIP, respectively.

Miscellaneous

Subfigures and plots were generated using GraphPad Prism (GraphPad Software, La Jolla, CA), Python Matplotlib library and R ggplot2. Cartoons of the dCas9 protein and sgRNA were adapted from images by the Innovative Genomics Institute, UC Berkeley and UCSF. All figures were assembled in Adobe Illustrator (Adobe, Inc.).

MAIN TEXT FIGURES

Figure 1 – A genome-wide CRISPRi screen reveals gene knockdowns that confer sensitivity or resistance to 5-aza-2'-deoxycytidine (decitabine).

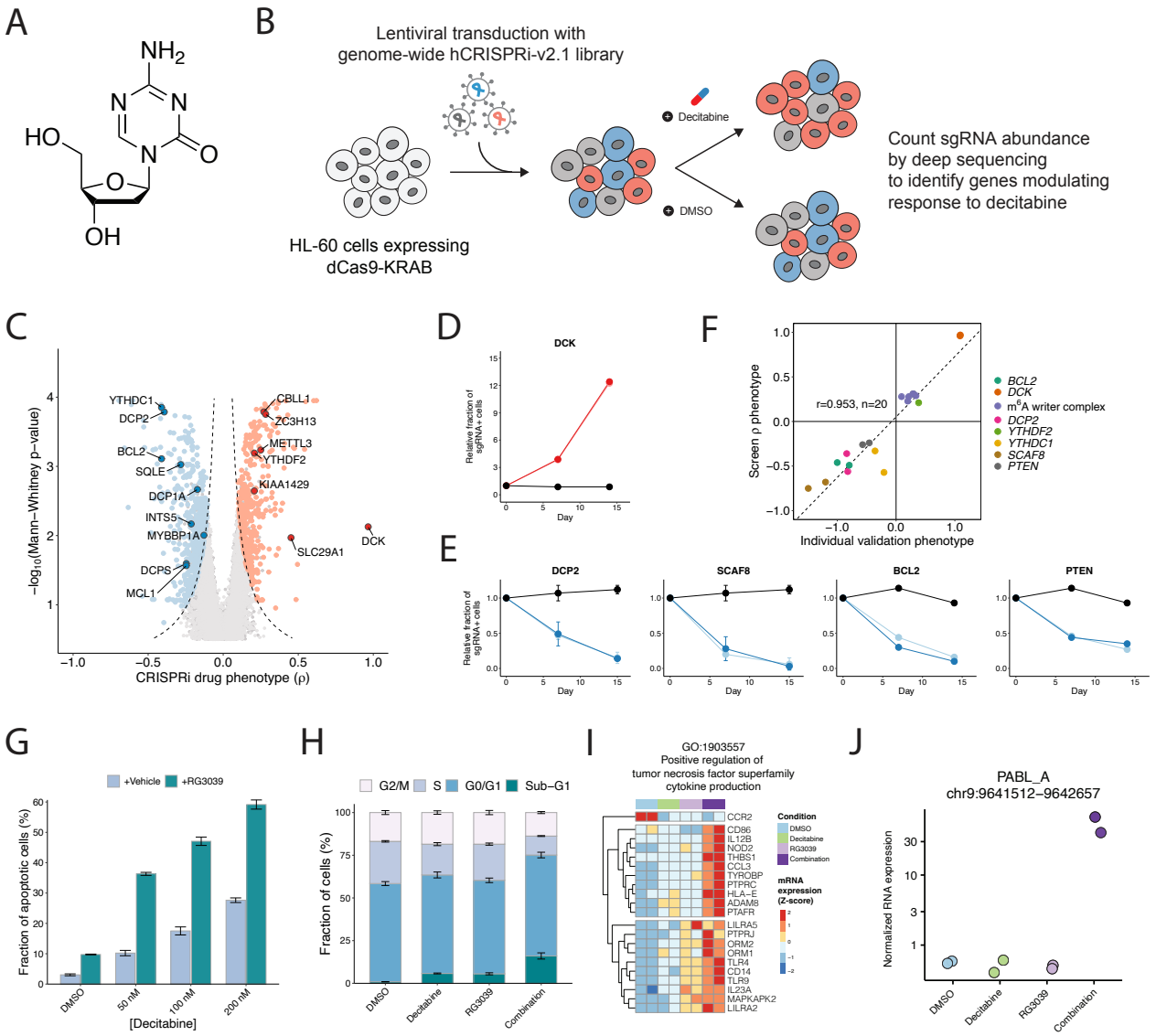

(**A**) The chemical structure of decitabine. (**B**) Schematic of a CRISPRi screen performed in HL-60 cells. (**C**) Volcano plot of gene-level rho (ρ) phenotypes and Mann-Whitney p-values. Negative rho values represent increased sensitivity to decitabine after knockdown, and positive rho values represent increased resistance. (**D**-**E**) Validation of top screen hits. HL-60i cells were transduced with a control sgRNA (black) or an active sgRNA (red or blue) and the relative proportion of sgRNA+ cells was observed over time. Data are shown as means ± SD, two sgRNAs per gene and two replicates per sgRNA. (**F**) Scatter plot showing the correlation between screen rho phenotype and validation phenotype (day 14-15 post-infection) for each validated sgRNA. (**G**) A cleaved caspase 3/7 assay shows the fraction of apoptotic HL-60 cells at day 5 following treatment with DMSO or decitabine ± RG3039. Data are shown as means ± SD for three replicates. (**H**) A cell cycle assay shows the fraction of HL-60 cells at different phases of the cell cycle at day 5 following treatment with DMSO or decitabine ± RG3039. Data are shown as means ± SD for three replicates. (**I**) Normalized counts for genes in GO:1903557 (Positive regulation of tumor necrosis factor superfamily cytokine production) upregulated upon decitabine and RG3039 treatment. (**J**) Normalized counts of an endogenous retrovirus strongly upregulated upon decitabine and RG3039 treatment.

Table 1 – HL-60 CRISPRi decitabine screen.
Gene-level phenotype scores and sgRNA protospacer sequences for validation assays.

Figure 2 – Decitabine treatment of WT HL-60 cells results in global m^{6}A hypermethylation.

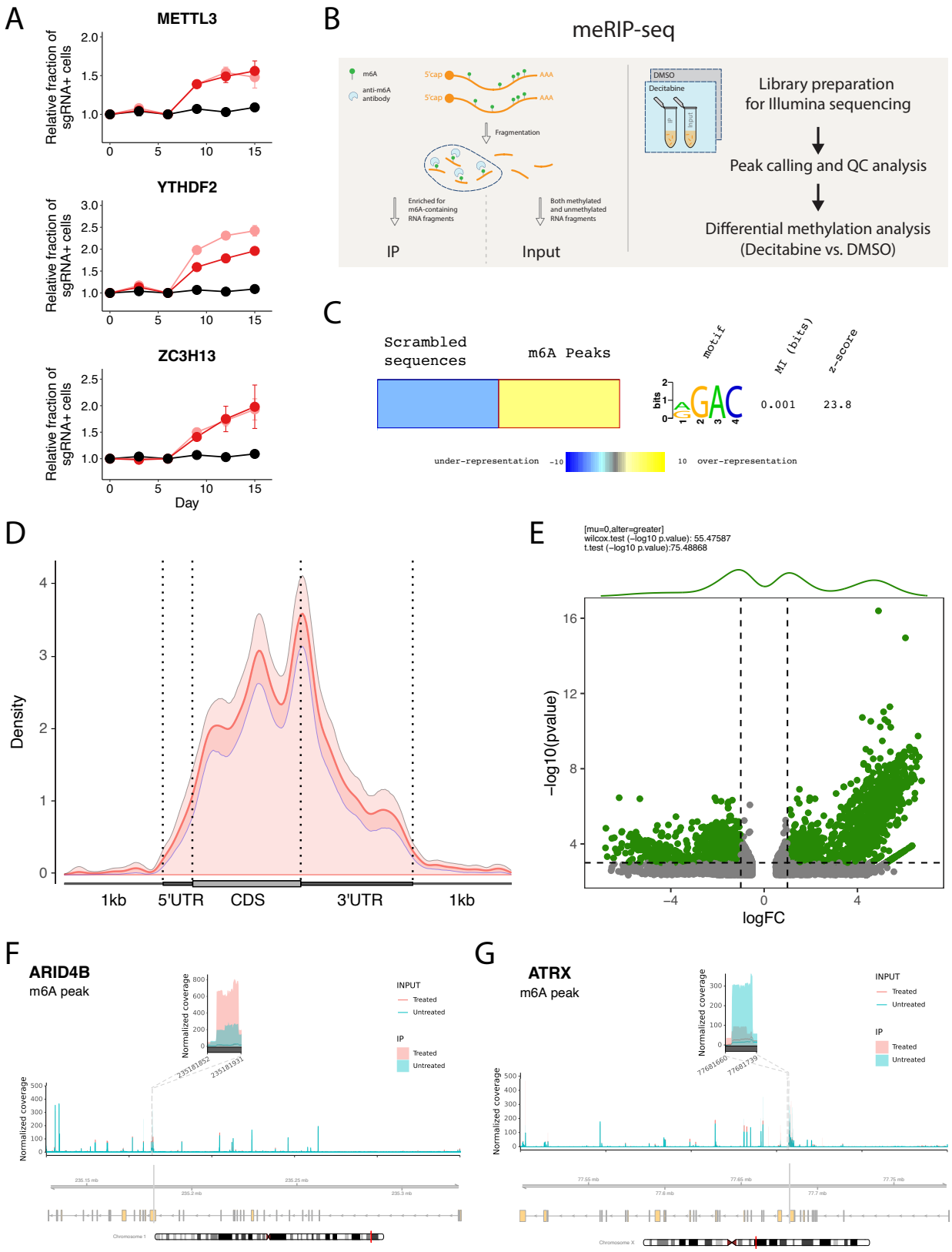

(**A**) Validation of CRISPRi decitabine screen hits shows that m^6A-reader/writer complex genes promote resistance to decitabine treatment upon knockdown in HL-60i cells. Data are shown as means ± SD, two sgRNAs per gene and two replicates per sgRNA. (**B**) Schematic of MeRIP-seq experimental design and computational workflow. (**C**) The FIRE algorithm (in non-discovery mode) shows the known m^6A motif RGAC ([AG]GAC) is enriched among predicted MeRIP-seq peaks relative to randomly generated sequences with similar dinucleotide frequencies. Data are shown as a heatmap, where yellow indicates over-representation and blue represents under-representation. Color intensity indicates the magnitude of enrichment. (**D**) Metagene plot of m^6A peak density demonstrates near end codon enrichment of m^6A peaks. (**E**) Differential methylation analysis shows significant hypermethylation in HL-60 cells treated with decitabine (relative to DMSO). (**F**) Coverage plots for select peaks predicted by the RADAR algorithm.

Table 2 – Differential RNA methylation analysis.
Differential analysis of MeRIP-seq data with RADAR (decitabine vs. DMSO).

Figure 3 – An analysis of differential gene expression and RNA stability across multiple AML cell lines and time points following decitabine treatment.

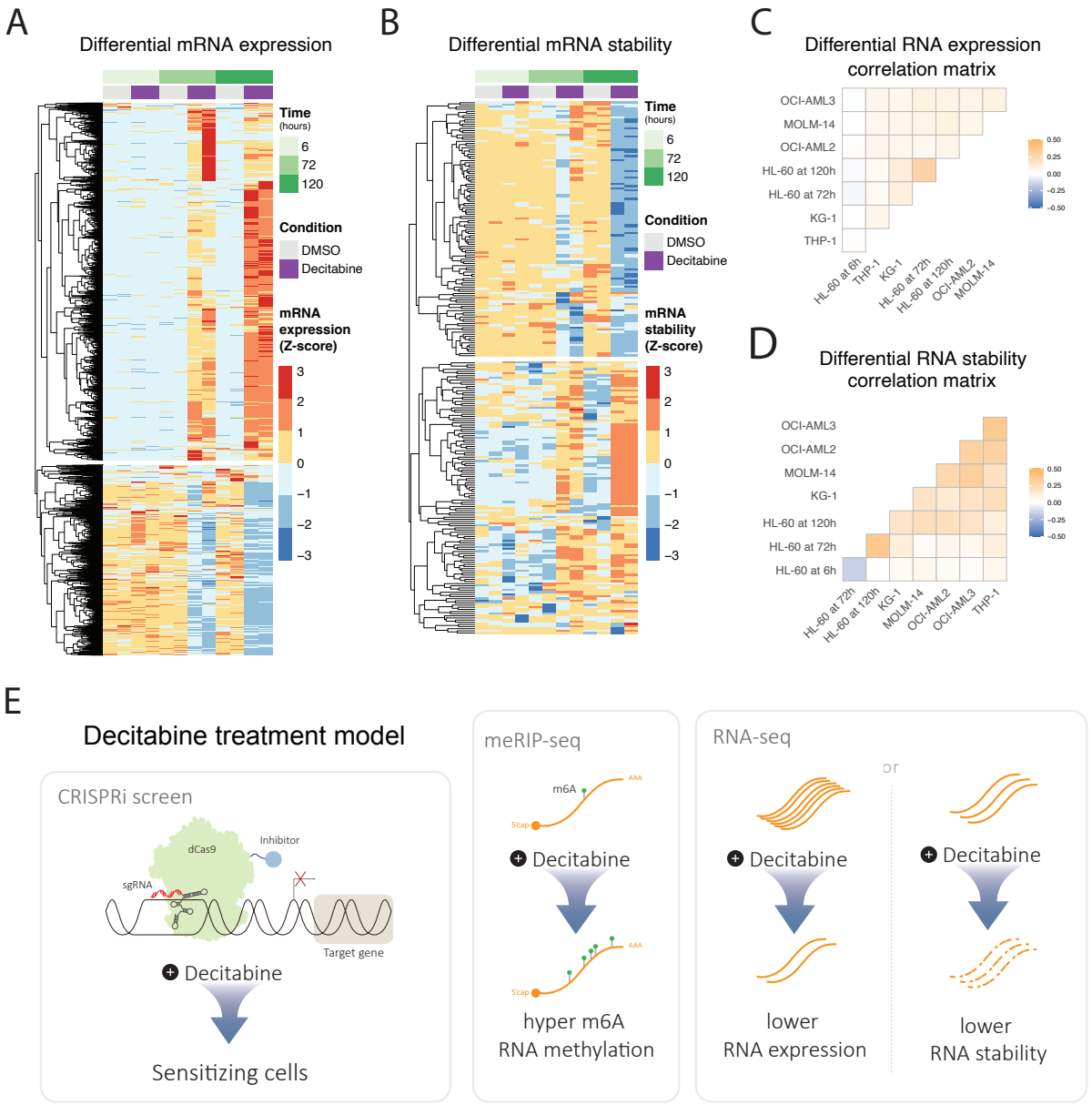

(**A**-**B**) RNA-seq reveals genes with significant changes in gene expression **(A)** or RNA stability **(B)** in HL-60 cells following treatment with decitabine vs. DMSO. Data are shown as heatmaps displaying counts (of two replicates) row-normalized into Z-scores, grouped by treatment condition and time. (**C**-**D**) RNA-seq shows varying degrees of concordance of (**C**) differential gene expression and (**D**) RNA stability across a panel of six AML cell lines treated with decitabine vs. DMSO. Data are shown as correlation matrices with Pearson's correlation coefficients. (**E**) A proposed model of decitabine induced changes in RNA dynamics integrating functional genomics data (i.e., CRISPRi genome-wide screen) with RNA-seq and MeRIP-seq data.

Figure 4 – Charting genes likely downregulated due to m^{6}A hypermethylation in HL-60 cells treated with decitabine and validating *INTS5* and *SQLE*.

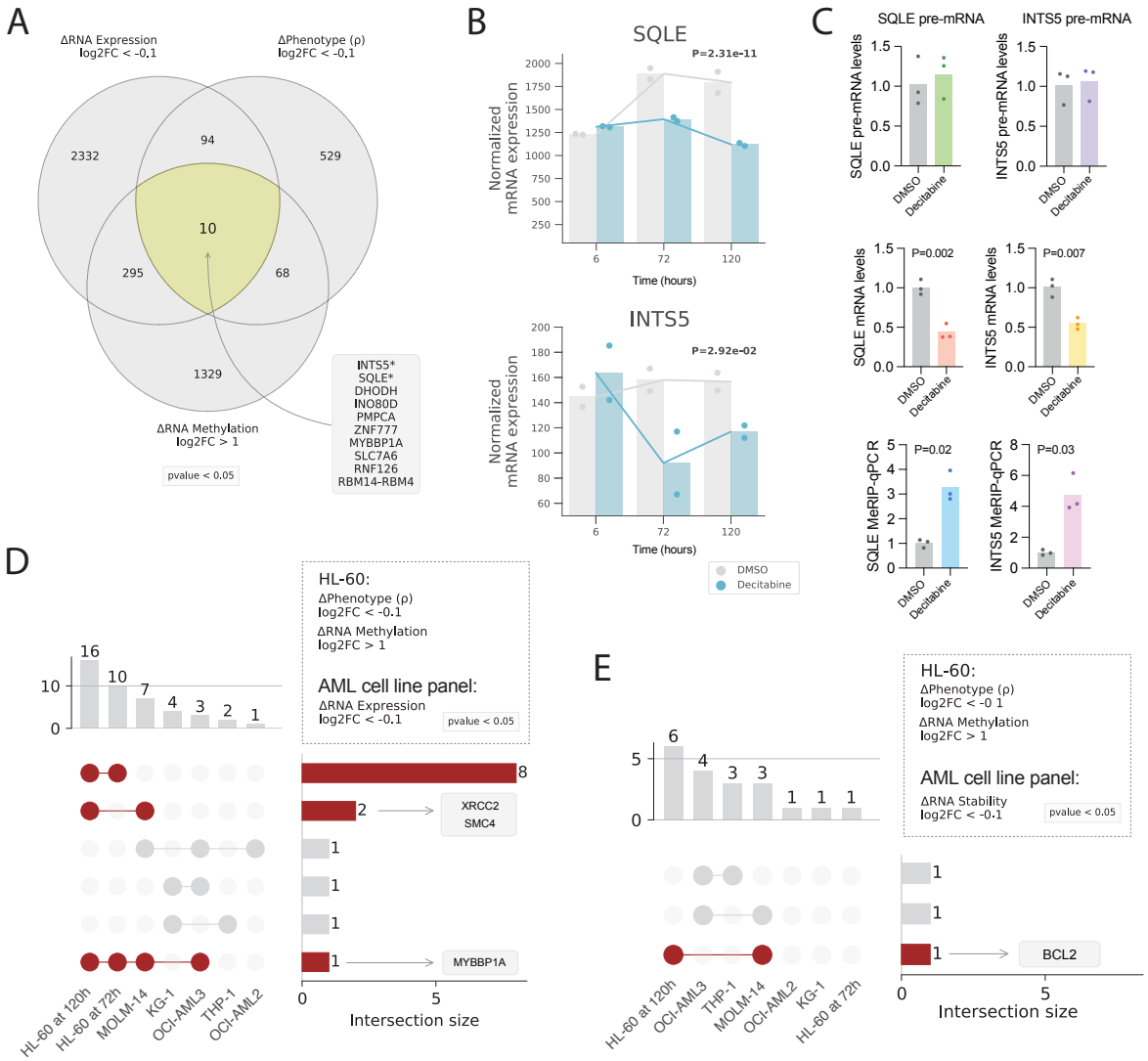

(**A**) Venn diagram visualization of three sets of genes across multiomics datasets (i.e., CRISPRi screen, RNA-seq and MeRIP-seq). We aimed to find an overlap between genes that (1) were sensitizing hits in our CRISPRi screen, (2) were RNA hypermethylated upon decitabine treatment and (3) were downregulated upon decitabine treatment. From this analysis, we selected *INTS5* and *SQLE* for downstream validation. (**B**) Normalized RNA-seq counts for *SQLE* and *INTS5* in HL-60 cells treated with decitabine vs. DMSO at 6 hours, 72 hours and 120 hours. Data are shown as two replicates and p-values were generated using a likelihood ratio test in DESeq2 comparing the decitabine and DMSO conditions at 72 hours. (**C**) MeRIP-qPCR validates our model of decitabine induced RNA hypermethylation and mRNA decay in *INTS5* and *SQLE*. Three sets of primers were designed to capture abundances of pre-mRNA (top), mature mRNA (middle) and predicted m^{6}A hypermethylated loci for each gene (bottom). Data are shown as three replicates, and one-tailed Mann-Whitney U-tests were used to assess statistical significance. (**D-E**) UpSet plots visualizing the intersection between genes which were (1) RNA hypermethylated upon decitabine treatment in HL-60 and (2) sensitizing hits in the HL-60 CRISPRi screen with genes downregulated (**D**) and RNA destabilized (**E**) across all six AML cell lines.

SUPPLEMENTARY FIGURES

Figure S1 – HL-60i validation and analysis of decitabine induced CpG DNA methylation changes in a public dataset.

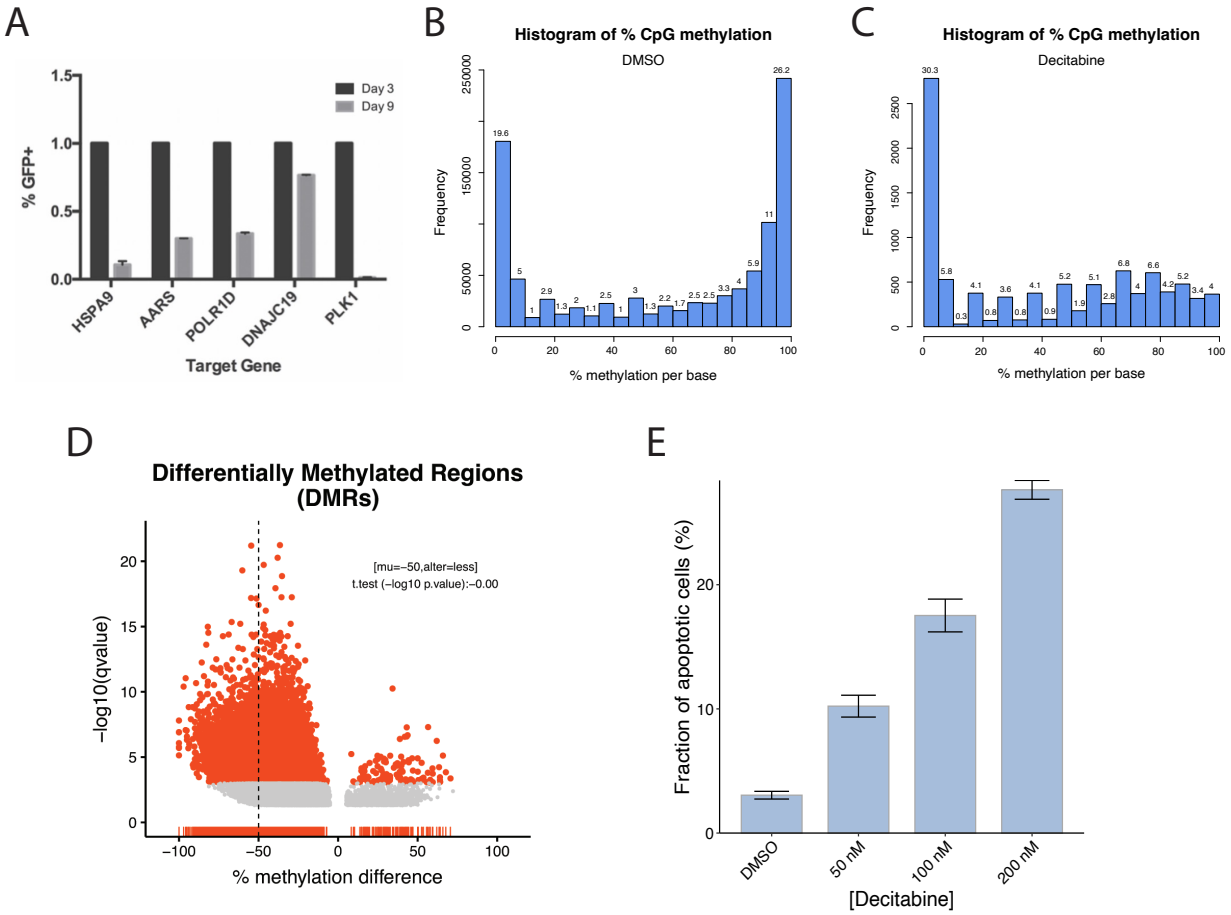

(**A**) Relative depletion of five sgRNAs targeting essential genes at day 9 (relative to day 3) in the HL-60i cell line, demonstrating functional CRISPRi activity. Each sgRNA was introduced into HL-60i via lentiviral transduction at infection rates of ~5–20%. GFP expression was used as a surrogate for sgRNA expression and the starting infection percentage for each sgRNA was normalized to 1. Cells were monitored over time via flow cytometry. Data are shown as means ± SD for two replicates. (**B-D**) Reanalysis of a public bisulfite-sequencing dataset (GSE149954) showing frequencies of base resolution CpG methylation in HL-60 cells treated with (**B**) DMSO or (**C**) 300 nM decitabine. (**D**) Volcano plot of differentially methylated regions (DMRs) comparing cells treated with decitabine vs. DMSO. A one-sided t-test shows statistically significant global hypomethylation of DNA CpG islands. (**E**) Apoptosis assay measuring cleaved caspase 3/7 at day 5 following treatment with DMSO or decitabine. Data are shown as means ± SD for three replicates. Data were derived from the same experiment as Figure 1G.

Figure S2 – HL-60 CRISPRi decitabine screen quality control metrics and enrichment analysis.

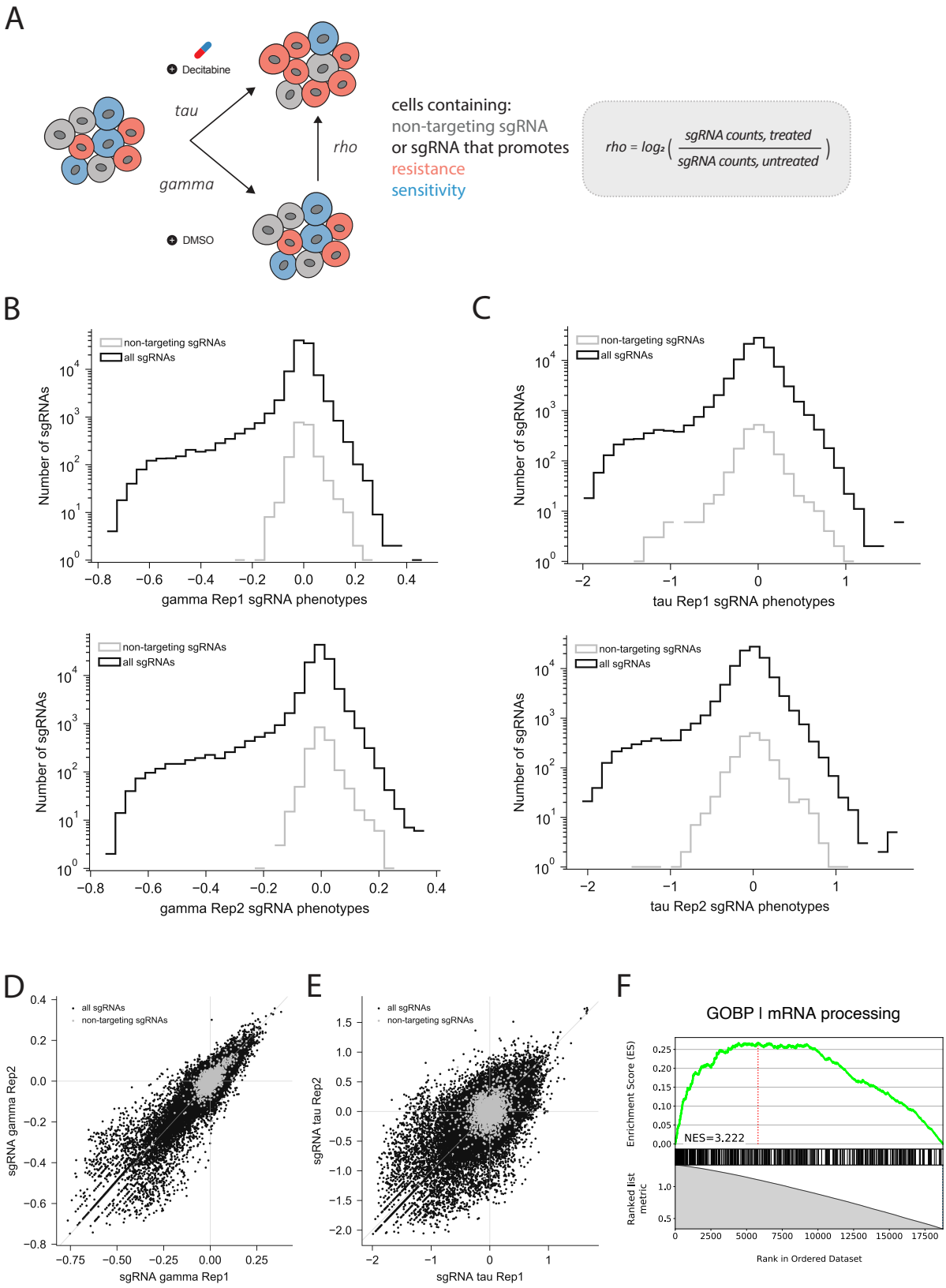

(**A**) Definition of CRISPRi screen phenotypes. (**B-C**) Distributions of sgRNA phenotypes per each screen replicate show many sgRNAs are highly active relative to the negative control sgRNA distribution. (**D-E**) Scatter plots show robust correlation between screen replicates for the gamma and tau phenotypes. Targeting and nontargeting sgRNAs included in the library are color coded black and gray, respectively. **(F)** GSEA plot showing enrichment of GO:0006397 (mRNA processing), a large gene ontology biological process (GOBP) term with a gene set size of 474. Genes were ranked by statistical significance (i.e., 1− Mann-Whitney p-value corresponding to each ρ phenotypes calculation). Normalized enrichment scores (NES) were calculated using the blitzGSEA Python package.

Table S1 – Pathway-level analysis of HL-60 CRISPRi screen phenotype scores.
Gene set enrichment analysis (GSEA) results using gene ontology (GO) gene sets. Two distinct GSEA analyses were performed (see methods).

Figure S3 – Characterizing synergy between decitabine and RG3039 in AML.

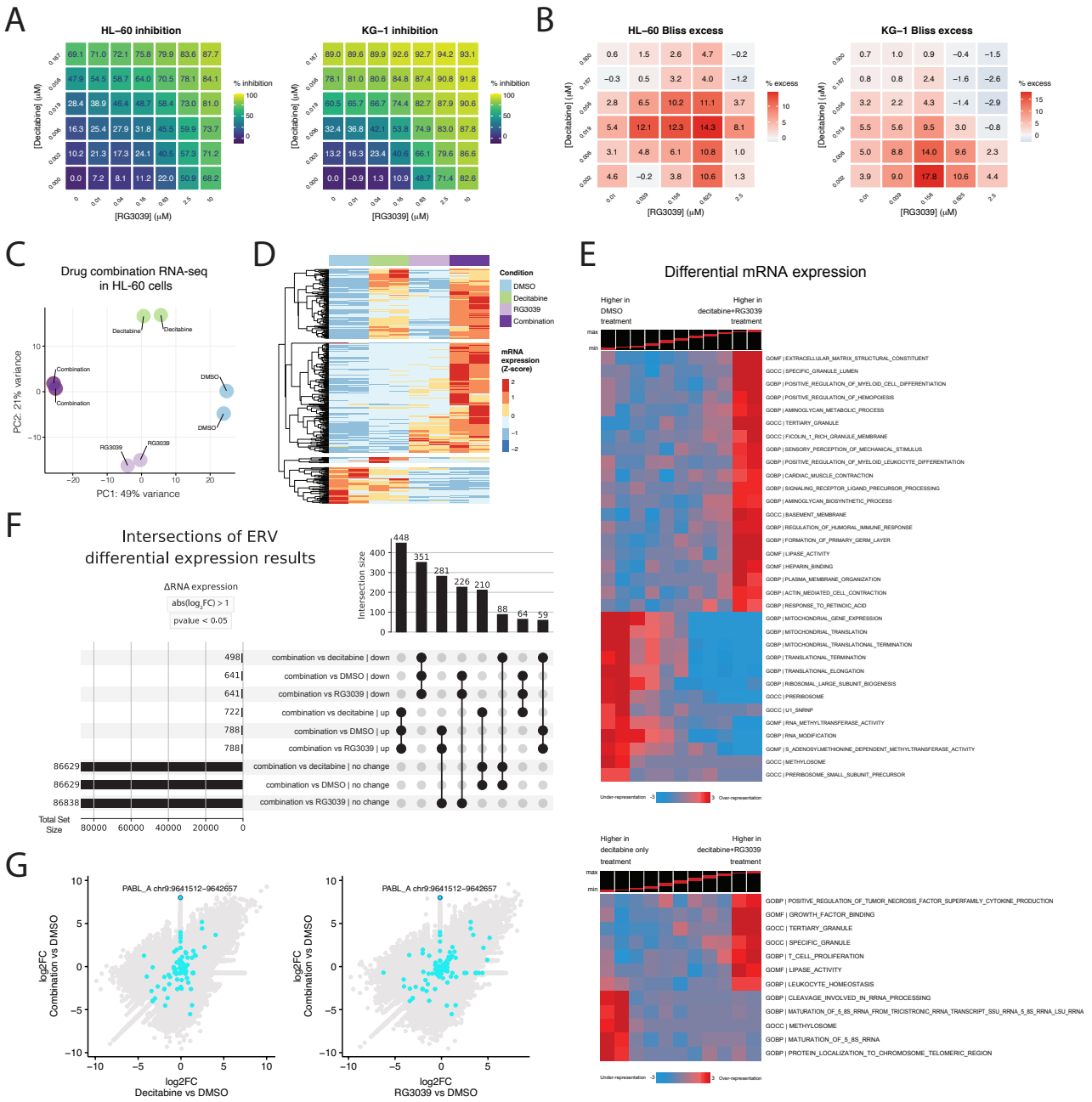

(**A**) Dose response matrices for HL-60 and KG-1 treated with dose combinations of decitabine and RG3039. Heatmaps display % cell inhibition (generated using a CellTiter-Glo assay; see methods for calculations) at each dose combination. Data are shown as means of two replicates. (**B**) Bliss excess scores (i.e., observed % cell inhibition – predicted % cell inhibition assuming Bliss independence; see methods for calculations) at each dose combination. Data are shown as means of two replicates. (**C**) PCA analysis of 3' RNA-seq (in duplicate) performed on HL-60 treated with DMSO, decitabine alone, RG3039 alone or both drugs. (**D**) DESeq2 analysis of 3' RNA-seq data reveals differentially expressed genes. Data are shown as a heatmap displaying counts row-normalized into Z-scores. (**E**) iPAGE analysis shows enrichment of gene ontologies (GOs) (heatmap rows) among differentially expressed genes (heatmap columns) in HL-60 treated with decitabine and RG3039 (top) or decitabine alone (bottom) vs. DMSO. Genes were first ranked based on log2FC from left to right and divided into eleven equally populated bins. Red boxes show enrichment and blue boxes show depletion. For each comparison, GOs are only shown if two of the first (i.e., up regulated GO) or last (i.e., down regulated GO) bins scored above 2. (**F**) An UpSet plot visualizes upregulated and downregulated endogenous retroviruses (ERVs) across treatment conditions. Upregulated ERVs (log2FC > 1 and p-value < 0.05) are labeled as "up", downregulated ERVs (log2FC < −1 and p-value < 0.05) are labeled as "down" and all other ERVs are labeled as "no change". (**G**) Scatter plots show differential ERV expression (as log2FC) in cells treated with decitabine or RG3039 alone (x-axis) vs. both drugs (y-axis). Pseudoautosomal boundary-like A (PABL_A) family members are highlighted in light blue. The labeled points correspond to the PABL_A chr9:9641512-9642657 locus, which is only upregulated in the decitabine and RG3039 drug combination (see also Figure 1J).

Figure S4 – Pathway-level changes in mRNA expression and stability associated with decitabine treatment in HL-60 cells.

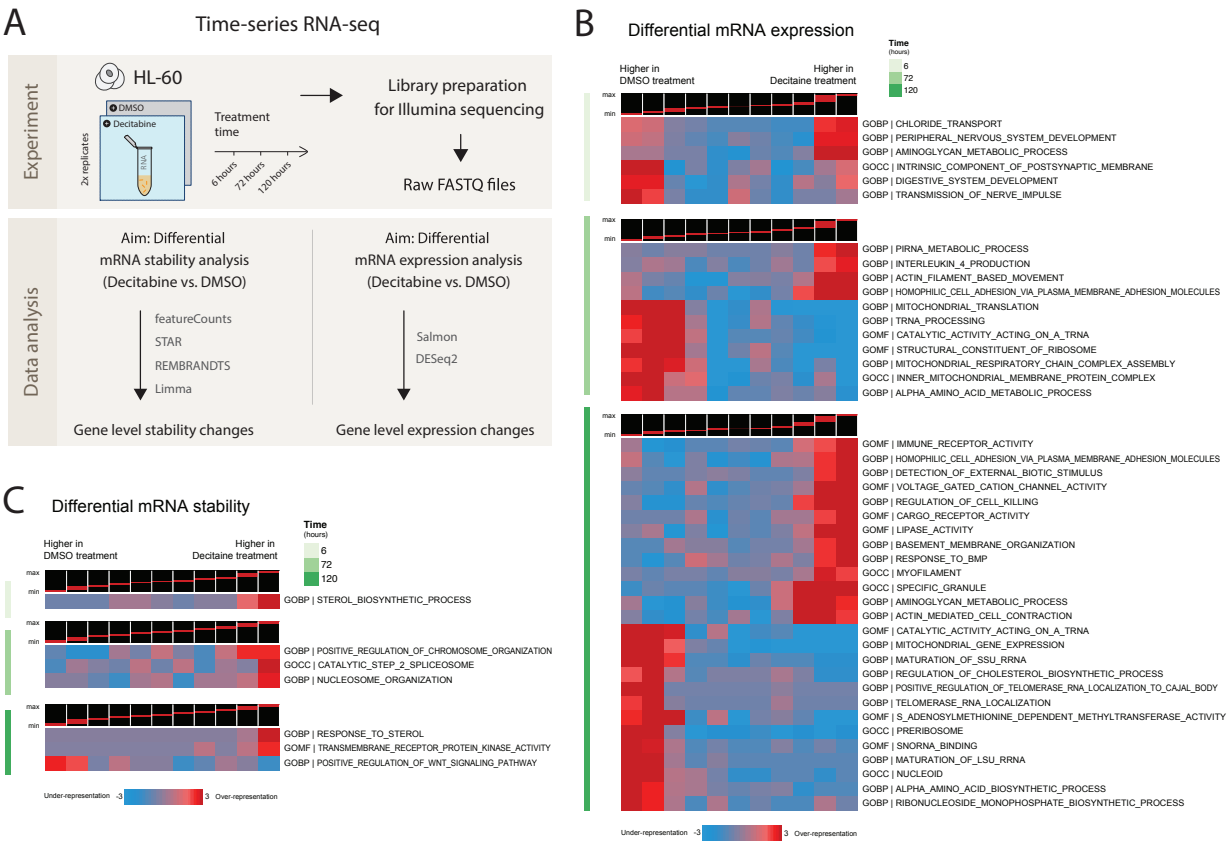

(**A**) Schematic of RNA-seq workflows in HL-60. (**B-C**) iPAGE analysis shows enrichment of GOs (heatmap rows) among changes in (**B**) RNA stability or (**C**) gene expression (heatmap columns; ranked and quantized into equal bins) in HL-60 cells treated with decitabine vs. DMSO at 6 hours (top), 72 hours (middle) or 120 hours (bottom). For each analysis, only enriched GOs are shown. RNA-seq experiments were performed in duplicate.

Figure S5 – Translational efficiency (TE) changes associated with decitabine treatment in HL-60 cells.

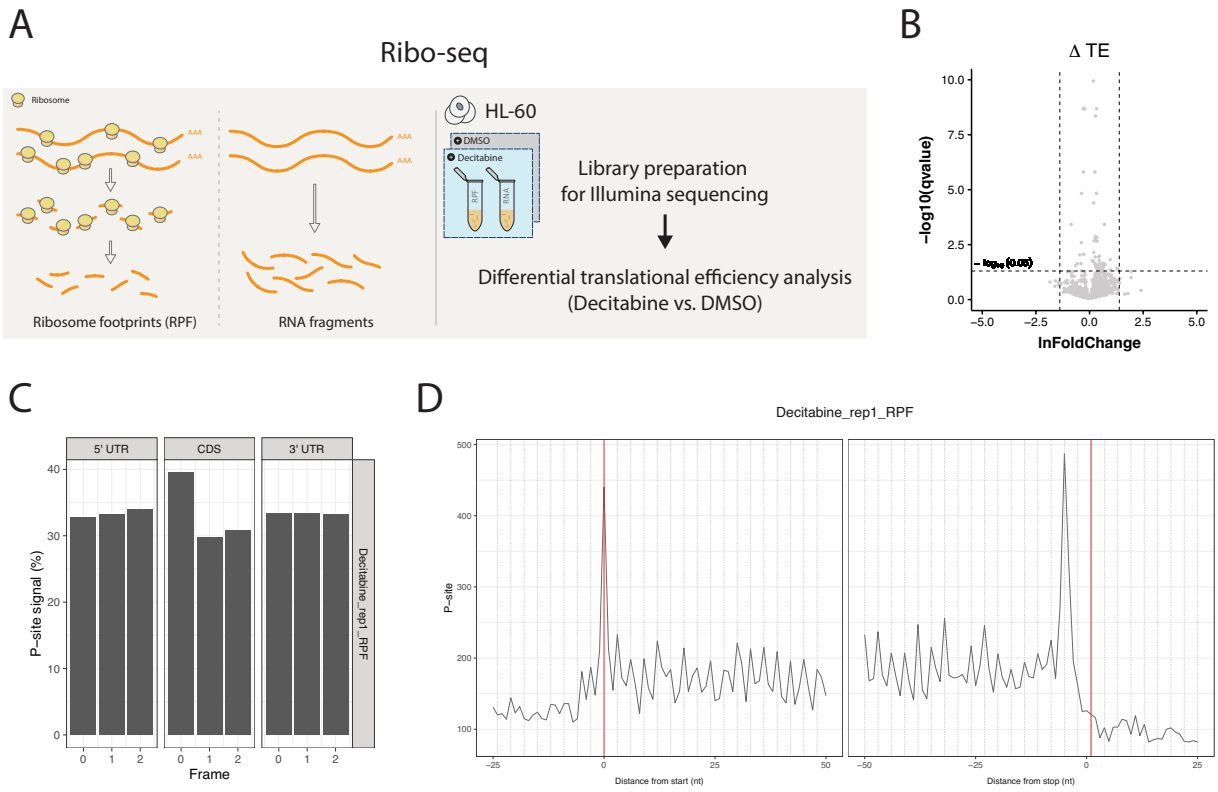

(**A**) Schematic of Ribo-seq. (**B**) Volcano plot visualization of Ribolog-calculated translational efficiency ratios (TERs) between the decitabine and DMSO conditions. (**C**) Bar plots showing enrichment of P-sites in the first frame of coding sequence (CDS) but not UTRs, consistent with ribosome protected fragments derived from protein coding mRNAs. (**D**) Ribosome occupancy profiles based on the 5' and 3' reads mapped to a reference codon for one sample (decitabine treated HL-60, single replicate).

Figure S6 – RNA m^{6}A hypermethylated peaks from MeRIP-seq in HL-60 following decitabine treatment.

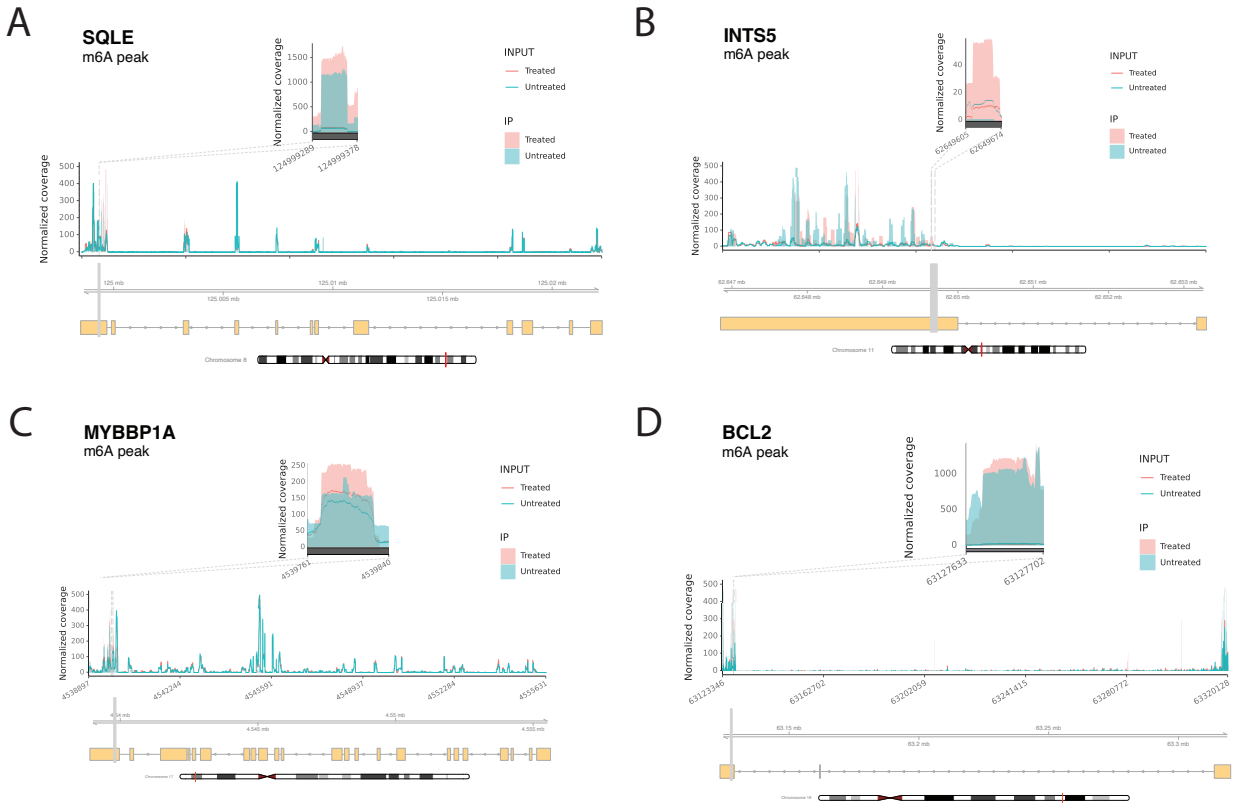

(**A**-**D**) Visualization of MeRIP-seq predicted m^{6}A peaks across mRNA transcripts of (**A**) *SQLE*, (**B**) *INTS5*, (**C**) *MYBBP1A* and (**D**) *BCL2* in HL-60 cells treated with decitabine vs. DMSO. Plots were generated using the RADAR and Gviz R packages.

REFERENCES

1. Flavahan, W. A., Gaskell, E. & Bernstein, B. E. Epigenetic plasticity and the hallmarks of cancer. *Science* **357**, eaal2380 (2017).
2. Ding, L. *et al.* Perspective on Oncogenic Processes at the End of the Beginning of Cancer Genomics. *Cell* **173**, 305-320.e10 (2018).
3. Tyner, J. W. *et al.* Functional genomic landscape of acute myeloid leukaemia. *Nature* **562**, 526–531 (2018).
4. Bates, S. E. Epigenetic Therapies for Cancer. *N. Engl. J. Med.* **383**, 650–663 (2020).
5. Ahuja, N., Sharma, A. R. & Baylin, S. B. Epigenetic Therapeutics: A New Weapon in the War Against Cancer. *Annu. Rev. Med.* **67**, 73–89 (2016).
6. Sato, T., Issa, J.-P. J. & Kropf, P. DNA Hypomethylating Drugs in Cancer Therapy. *Cold Spring Harb. Perspect. Med.* **7**, a026948 (2017).
7. Middeke, J. M. *et al.* Decitabine treatment in 311 patients with acute myeloid leukemia: outcome and impact of TP53 mutations - a registry based analysis. *Leuk. Lymphoma* **62**, 1432–1440 (2021).
8. Welch, J. S. *et al.* TP53 and Decitabine in Acute Myeloid Leukemia and Myelodysplastic Syndromes. *N. Engl. J. Med.* **375**, 2023–2036 (2016).
9. DiNardo, C. D. *et al.* Venetoclax combined with decitabine or azacitidine in treatment-naive, elderly patients with acute myeloid leukemia. *Blood* **133**, 7–17 (2019).
10. Brocks, D. *et al.* DNMT and HDAC inhibitors induce cryptic transcription start sites encoded in long terminal repeats. *Nat. Genet.* **49**, 1052–1060 (2017).
11. Mehdipour, P. *et al.* Epigenetic therapy induces transcription of inverted SINEs and ADAR1 dependency. *Nature* **588**, 169–173 (2020).
12. Ku, Y. *et al.* Noncanonical immune response to the inhibition of DNA methylation by Staufen1 via stabilization of endogenous retrovirus RNAs. *Proc. Natl. Acad. Sci. U. S. A.* **118**, e2016289118 (2021).
13. Roulois, D. *et al.* DNA-Demethylating Agents Target Colorectal Cancer Cells by Inducing Viral Mimicry by Endogenous Transcripts. *Cell* **162**, 961–973 (2015).
14. Chiappinelli, K. B. *et al.* Inhibiting DNA Methylation Causes an Interferon Response in Cancer via dsRNA Including Endogenous Retroviruses. *Cell* **162**, 974–986 (2015).
15. Jones, P. A. & Taylor, S. M. Cellular differentiation, cytidine analogs and DNA methylation. *Cell* **20**, 85–93 (1980).
16. Stresemann, C. & Lyko, F. Modes of action of the DNA methyltransferase inhibitors azacytidine and decitabine. *Int. J. Cancer* **123**, 8–13 (2008).
17. Wu, P. *et al.* The hENT1 and DCK genes underlie the decitabine response in patients with myelodysplastic syndrome. *Leuk. Res.* **39**, 216–220 (2015).
18. Qin, T., Jelinek, J., Si, J., Shu, J. & Issa, J.-P. J. Mechanisms of resistance to 5-aza-2'-deoxycytidine in human cancer cell lines. *Blood* **113**, 659–667 (2009).
19. Bogenberger, J. M. *et al.* Ex vivo activity of BCL-2 family inhibitors ABT-199 and ABT-737 combined with 5-azacytidine in myeloid malignancies. *Leuk. Lymphoma* **56**, 226–229 (2015).
20. Tsao, T. *et al.* Concomitant inhibition of DNA methyltransferase and BCL-2 protein function synergistically induce mitochondrial apoptosis in acute myelogenous leukemia cells. *Ann. Hematol.* **91**, 1861–1870 (2012).
21. Sorrentino, V. G. *et al.* Hypomethylating Chemotherapeutic Agents as Therapy for Myelodysplastic Syndromes and Prevention of Acute Myeloid Leukemia. *Pharm. Basel Switz.* **14**, 641 (2021).

22. Gilbert, L. A. *et al.* Genome-Scale CRISPR-Mediated Control of Gene Repression and Activation. *Cell* **159**, 647–661 (2014).
23. Horlbeck, M. A. *et al.* Compact and highly active next-generation libraries for CRISPR-mediated gene repression and activation. *eLife* **5**, e19760 (2016).
24. Shareef, S. J. *et al.* Extended-representation bisulfite sequencing of gene regulatory elements in multiplexed samples and single cells. *Nat. Biotechnol.* **39**, 1086–1094 (2021).
25. Cashen, A. F., Shah, A. K., Todt, L., Fisher, N. & DiPersio, J. Pharmacokinetics of decitabine administered as a 3-h infusion to patients with acute myeloid leukemia (AML) or myelodysplastic syndrome (MDS). *Cancer Chemother. Pharmacol.* **61**, 759–766 (2008).
26. Orta, M. L. *et al.* 5-Aza-2'-deoxycytidine causes replication lesions that require Fanconi anemia-dependent homologous recombination for repair. *Nucleic Acids Res.* **41**, 5827–5836 (2013).
27. Tsai, H.-C. *et al.* Transient low doses of DNA-demethylating agents exert durable antitumor effects on hematological and epithelial tumor cells. *Cancer Cell* **21**, 430–446 (2012).
28. Lachmann, A., Xie, Z. & Ma'ayan, A. blitzGSEA: Efficient computation of Gene Set Enrichment Analysis through Gamma distribution approximation. *Bioinforma. Oxf. Engl.* **38**, 2356–2357 (2022).
29. Dutkowski, J. *et al.* A gene ontology inferred from molecular networks. *Nat. Biotechnol.* **31**, 38–45 (2013).
30. Harris, M. A. *et al.* The Gene Ontology (GO) database and informatics resource. *Nucleic Acids Res.* **32**, D258-261 (2004).
31. Yamauchi, T. *et al.* Genome-wide CRISPR-Cas9 Screen Identifies Leukemia-Specific Dependence on a Pre-mRNA Metabolic Pathway Regulated by DCPS. *Cancer Cell* **33**, 386-400.e5 (2018).
32. Zhou, M., Bail, S., Plasterer, H. L., Rusche, J. & Kiledjian, M. DcpS is a transcript-specific modulator of RNA in mammalian cells. *RNA N. Y. N* **21**, 1306–1312 (2015).
33. Liu, H., Rodgers, N. D., Jiao, X. & Kiledjian, M. The scavenger mRNA decapping enzyme DcpS is a member of the HIT family of pyrophosphatases. *EMBO J.* **21**, 4699–4708 (2002).
34. Li, H. *et al.* Immune regulation by low doses of the DNA methyltransferase inhibitor 5-azacitidine in common human epithelial cancers. *Oncotarget* **5**, 587–598 (2014).
35. Fukagawa, T. *et al.* A boundary of long-range G + C% mosaic domains in the human MHC locus: pseudoautosomal boundary-like sequence exists near the boundary. *Genomics* **25**, 184–191 (1995).
36. Waggoner, M., Katsetos, J., Thomas, E., Galinsky, I. & Fox, H. Practical Management of the Venetoclax-Treated Patient in Chronic Lymphocytic Leukemia and Acute Myeloid Leukemia. *J. Adv. Pract. Oncol.* **13**, 400–415 (2022).
37. Zeng, Y. *et al.* Refined RIP-seq protocol for epitranscriptome analysis with low input materials. *PLoS Biol.* **16**, e2006092 (2018).
38. Elemento, O., Slonim, N. & Tavazoie, S. A universal framework for regulatory element discovery across all genomes and data types. *Mol. Cell* **28**, 337–350 (2007).
39. Alarcón, C. R., Lee, H., Goodarzi, H., Halberg, N. & Tavazoie, S. F. N6-methyladenosine marks primary microRNAs for processing. *Nature* **519**, 482–485 (2015).
40. Meyer, K. D. *et al.* Comprehensive analysis of mRNA methylation reveals enrichment in 3' UTRs and near stop codons. *Cell* **149**, 1635–1646 (2012).
41. Zhang, Z. *et al.* RADAR: differential analysis of MeRIP-seq data with a random effect model. *Genome Biol.* **20**, 294 (2019).

42. Zaccara, S., Ries, R. J. & Jaffrey, S. R. Reading, writing and erasing mRNA methylation. *Nat. Rev. Mol. Cell Biol.* **20**, 608–624 (2019).
43. Fish, L. *et al.* Nuclear TARBP2 Drives Oncogenic Dysregulation of RNA Splicing and Decay. *Mol. Cell* **75**, 967-981.e9 (2019).
44. Wang, X. *et al.* N6-methyladenosine-dependent regulation of messenger RNA stability. *Nature* **505**, 117–120 (2014).
45. Wang, X. *et al.* N(6)-methyladenosine Modulates Messenger RNA Translation Efficiency. *Cell* **161**, 1388–1399 (2015).
46. Zhou, J. *et al.* Dynamic m(6)A mRNA methylation directs translational control of heat shock response. *Nature* **526**, 591–594 (2015).
47. Xu, W. & Shen, H. When RNA methylation meets DNA methylation. *Nat. Genet.* **54**, 1261–1262 (2022).
48. Kan, R. L., Chen, J. & Sallam, T. Crosstalk between epitranscriptomic and epigenetic mechanisms in gene regulation. *Trends Genet. TIG* **38**, 182–193 (2022).
49. Lee, J.-H. *et al.* Enhancer RNA m6A methylation facilitates transcriptional condensate formation and gene activation. *Mol. Cell* **81**, 3368-3385.e9 (2021).
50. Deng, S. *et al.* RNA m6A regulates transcription via DNA demethylation and chromatin accessibility. *Nat. Genet.* **54**, 1427–1437 (2022).
51. Love, M. I., Huber, W. & Anders, S. Moderated estimation of fold change and dispersion for RNA-seq data with DESeq2. *Genome Biol.* **15**, 550 (2014).
52. Soneson, C., Love, M. I. & Robinson, M. D. Differential analyses for RNA-seq: transcript-level estimates improve gene-level inferences. *F1000Research* **4**, 1521 (2015).
53. Patro, R., Duggal, G., Love, M. I., Irizarry, R. A. & Kingsford, C. Salmon provides fast and bias-aware quantification of transcript expression. *Nat. Methods* **14**, 417–419 (2017).
54. Dobin, A. *et al.* STAR: ultrafast universal RNA-seq aligner. *Bioinforma. Oxf. Engl.* **29**, 15–21 (2013).
55. Ritchie, M. E. *et al.* limma powers differential expression analyses for RNA-sequencing and microarray studies. *Nucleic Acids Res.* **43**, e47 (2015).
56. Alkallas, R., Fish, L., Goodarzi, H. & Najafabadi, H. S. Inference of RNA decay rate from transcriptional profiling highlights the regulatory programs of Alzheimer's disease. *Nat. Commun.* **8**, 909 (2017).
57. Goodarzi, H., Elemento, O. & Tavazoie, S. Revealing global regulatory perturbations across human cancers. *Mol. Cell* **36**, 900–911 (2009).
58. Mao, Y. *et al.* m6A in mRNA coding regions promotes translation via the RNA helicase-containing YTHDC2. *Nat. Commun.* **10**, 5332 (2019).
59. He, P. C. & He, C. m6 A RNA methylation: from mechanisms to therapeutic potential. *EMBO J.* **40**, e105977 (2021).
60. Fu, Y., Dominissini, D., Rechavi, G. & He, C. Gene expression regulation mediated through reversible m^6A RNA methylation. *Nat. Rev. Genet.* **15**, 293–306 (2014).
61. Garcia-Bermudez, J. *et al.* Squalene accumulation in cholesterol auxotrophic lymphomas prevents oxidative cell death. *Nature* **567**, 118–122 (2019).
62. Yan, A., Jia, Z., Qiao, C., Wang, M. & Ding, X. Cholesterol metabolism in drug-resistant cancer (Review). *Int. J. Oncol.* **57**, 1103–1115 (2020).

63. Li, Y. & Kiledjian, M. Regulation of mRNA decapping. *Wiley Interdiscip. Rev. RNA* **1**, 253–265 (2010).
64. Grudzien-Nogalska, E. & Kiledjian, M. New insights into decapping enzymes and selective mRNA decay. *Wiley Interdiscip. Rev. RNA* **8**, (2017).
65. Ng, C. K. L. *et al.* Loss of the scavenger mRNA decapping enzyme DCPS causes syndromic intellectual disability with neuromuscular defects. *Hum. Mol. Genet.* **24**, 3163–3171 (2015).
66. Bassik, M. C. *et al.* A systematic mammalian genetic interaction map reveals pathways underlying ricin susceptibility. *Cell* **152**, 909–922 (2013).
67. Kampmann, M., Bassik, M. C. & Weissman, J. S. Functional genomics platform for pooled screening and generation of mammalian genetic interaction maps. *Nat. Protoc.* **9**, 1825–1847 (2014).
68. Kampmann, M., Bassik, M. C. & Weissman, J. S. Integrated platform for genome-wide screening and construction of high-density genetic interaction maps in mammalian cells. *Proc. Natl. Acad. Sci. U. S. A.* **110**, E2317-2326 (2013).
69. Liberzon, A. *et al.* Molecular signatures database (MSigDB) 3.0. *Bioinforma. Oxf. Engl.* **27**, 1739–1740 (2011).
70. Liberzon, A. *et al.* The Molecular Signatures Database (MSigDB) hallmark gene set collection. *Cell Syst.* **1**, 417–425 (2015).
71. Krueger, F., James, F., Ewels, P., Afyounian, E. & Schuster-Boeckler, B. FelixKrueger/TrimGalore: v0.6.7 - DOI via Zenodo. (2021) doi:10.5281/ZENODO.5127899.
72. Krueger, F. & Andrews, S. R. Bismark: a flexible aligner and methylation caller for Bisulfite-Seq applications. *Bioinforma. Oxf. Engl.* **27**, 1571–1572 (2011).
73. Akalin, A. *et al.* methylKit: a comprehensive R package for the analysis of genome-wide DNA methylation profiles. *Genome Biol.* **13**, R87 (2012).
74. Bliss, C. I. The calculation of microbial assays. *Bacteriol. Rev.* **20**, 243–258 (1956).
75. Frankish, A. *et al.* GENCODE 2021. *Nucleic Acids Res.* **49**, D916–D923 (2021).
76. Law, C. W. *et al.* A guide to creating design matrices for gene expression experiments. *F1000Research* **9**, 1444 (2020).
77. Liao, Y., Smyth, G. K. & Shi, W. featureCounts: an efficient general purpose program for assigning sequence reads to genomic features. *Bioinforma. Oxf. Engl.* **30**, 923–930 (2014).
78. Paces, J., Pavlícek, A. & Paces, V. HERVd: database of human endogenous retroviruses. *Nucleic Acids Res.* **30**, 205–206 (2002).
79. Paces, J. *et al.* HERVd: the Human Endogenous RetroViruses Database: update. *Nucleic Acids Res.* **32**, D50 (2004).
80. Lex, A., Gehlenborg, N., Strobelt, H., Vuillemot, R. & Pfister, H. UpSet: Visualization of Intersecting Sets. *IEEE Trans. Vis. Comput. Graph.* **20**, 1983–1992 (2014).
81. Cui, X. *et al.* Guitar: An R/Bioconductor Package for Gene Annotation Guided Transcriptomic Analysis of RNA-Related Genomic Features. *BioMed Res. Int.* **2016**, 8367534 (2016).
82. Hahne, F. & Ivanek, R. Visualizing Genomic Data Using Gviz and Bioconductor. *Methods Mol. Biol. Clifton NJ* **1418**, 335–351 (2016).
83. Meng, J. *et al.* A protocol for RNA methylation differential analysis with MeRIP-Seq data and exomePeak R/Bioconductor package. *Methods San Diego Calif* **69**, 274–281 (2014).
84. Sims, D. *et al.* CGAT: computational genomics analysis toolkit. *Bioinforma. Oxf. Engl.* **30**, 1290–1291 (2014).

85. Quinlan, A. R. & Hall, I. M. BEDTools: a flexible suite of utilities for comparing genomic features. *Bioinforma. Oxf. Engl.* **26**, 841–842 (2010).
86. McGlincy, N. J. & Ingolia, N. T. Transcriptome-wide measurement of translation by ribosome profiling. *Methods San Diego Calif* **126**, 112–129 (2017).
87. Martin, M. Cutadapt removes adapter sequences from high-throughput sequencing reads. *EMBnet.journal* **17**, 10 (2011).
88. Kathryn Rozen-Gagnon, Thomas Carroll, Ji-Dung Luo, Wei Wang, & Troels Scheel. CLIPflexR: CLIP tools and wrappers in R. (2022).
89. Smith, T., Heger, A. & Sudbery, I. UMI-tools: modeling sequencing errors in Unique Molecular Identifiers to improve quantification accuracy. *Genome Res.* **27**, 491–499 (2017).
90. Langmead, B. & Salzberg, S. L. Fast gapped-read alignment with Bowtie 2. *Nat. Methods* **9**, 357–359 (2012).
91. Li, H. *et al.* The Sequence Alignment/Map format and SAMtools. *Bioinforma. Oxf. Engl.* **25**, 2078–2079 (2009).
92. Cunningham, F. *et al.* Ensembl 2022. *Nucleic Acids Res.* **50**, D988–D995 (2022).
93. Navickas, A. *et al. An mRNA processing pathway suppresses metastasis by governing translational control from the nucleus*. http://biorxiv.org/lookup/doi/10.1101/2021.10.04.463118 (2021) doi:10.1101/2021.10.04.463118.